THE ÅNGSTRÖM LASER - A UNIQUE MEDIUM-SCALE X-RAY FACILITY FOR SUSTAINABLE MATERIALS SCIENCE

Executive summary

Vision: Developments of new research areas and breakthroughs in science are often linked to the development of new instrumentation. Using superconducting accelerator technology, we propose to build the Ångström Laser (see Fig. 1): a source of high repetition rate femtosecond flashes of X-ray radiation that enable exploring materials on the ultimate quantum level of moving atoms and electrons. The Ångström Laser will be a discovery machine for new materials and novel sustainable technologies.

Mission: The Ångström Laser will represent a novel research infrastructure for both basic and need-driven materials science for sustainability. It will provide unique capabilities not available at the already existing national and international X-ray facilities and it will enable new approaches to materials characterization and discovery. It will provide user groups with direct access to the dynamically evolving microscopic processes that determine the functionality of materials in

1. Heterogeneous Catalysis: Creating a sustainable chemical industry
2. Molecular catalysis: Converting solar into chemical energy
3. Operando processes in photovoltaic materials
4. Understanding the time-resolved charge transfer in electrochemical processes
5. Materials for hydrogen storage
6. Energy efficient control of quantum materials properties
7. Towards energy-efficient information technology with topological materials

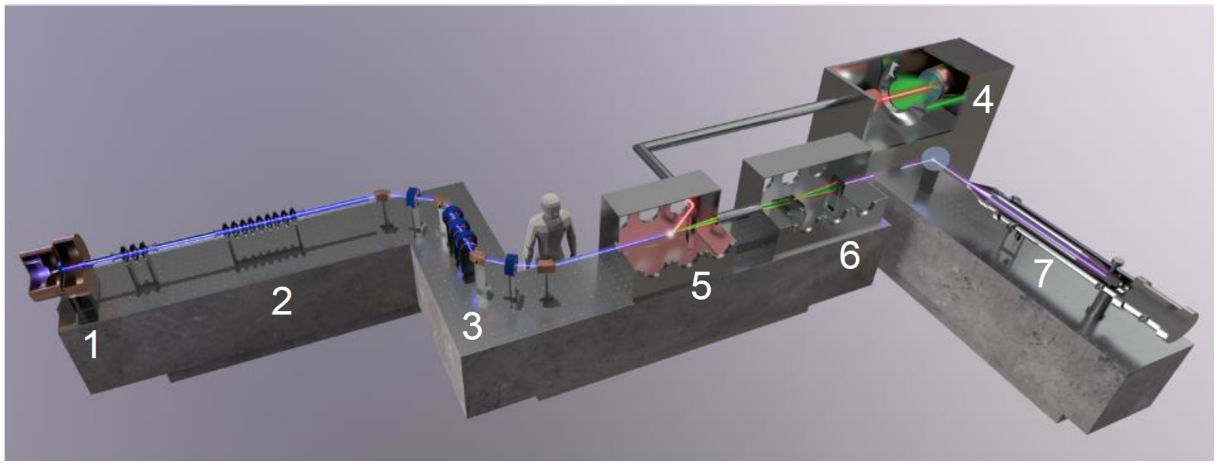

Figure 1: Illustration of the Ångström Laser based on a superconducting electron accelerator and an optical undulator. The baseline design described in this conceptual design report does not contain the S-shaped bunch compressor 3 illustrated here. Main components from left to right: 1 Electron gun, 2 superconducting accelerator cavity, 3 bunch compressor, 4 optical laser for optical undulator, 5 optical undulator, 6 X-ray monochromator, 7 photoelectron spectrometer. This illustration only depicts a photoelectron spectroscopy end station (transient absorption and diffraction are not shown).

Strategy: The Ångström Laser is a unique medium-scale X-ray facility that fills the capa-

bility gap between synchrotrons and X-ray Free Electron Lasers. The conceptual design simulations (see Table 1) promise a flux of 10^9 photons/s in a broad energy bandwidth ideally suited for time-resolved X-ray absorption spectroscopy and X-ray scattering, and 10^8 photons/s in a narrow energy bandwidth ideal for time-resolved X-ray photoemission spectroscopy. With photon energies of 2-13 keV, the Ångström Laser will access X-ray absorption edges in transient absorption of important elements in catalysis and make possible depth profiling in diffraction to access interfaces in materials. With its high repetition rate of 100 kHz of the femtosecond X-ray flashes, the Ångström Laser will enable probing functional materials as their properties evolve on intrisic time- and lengthscales. Resolving materials' properties in time complements studies of steady states of materials at the MAX IV synchrotron. The Ångström Laser adds capabilities and capacities with femtosecond tender and hard X-ray pulses that are currently only available at X-ray free electron laser facilities such as the European XFEL in Hamburg where Sweden provides the largest per capita user community. The Ångström Laser will provide Swedish users with a cost-effective alternative and, interestingly, with more access to beamtime than is possible at the European XFEL were access is shared with many more user groups. In addition, with the Ångström Laser, a new sample can be examined next door right after sample synthesis to uniquely inform on a new synthesis step and then create yet another new sample to be examined at the Ångström Laser, etc. By bringing this new ultrafast X-ray characterization capability to university groups and small companies, the resulting iterative sample synthesis-characterization loops can accelerate the discovery cycle of materials.

Table 1: Projected X-ray parameters of the Ångström Laser (see chapter 3) at the end of the optical undulator source, at the sample in the broadband X-ray beamline branch and at the sample position in the monochromatic beamline.

X-ray output parameters	**Optical undulator**	**Broadband beamline (at the sample)**	**Monochromatic beamline (at the sample)**
X-ray energy range	2-13 keV	2-13 keV	2-8 keV
X-ray energy bandwidth	1%	1%	$\sim$0.02%
X-ray pulse duration (FWHM)	$<$200 fs	$<$200 fs	$<$200 fs
Flux (s^{-1}) at 100 kHz rep. rate	10^{10}	10^9	10^7-10^8
X-ray spot size, (FWHM)	8.0 µm	35 µm	41 µm

Goal: The national setting of the Ångström Laser will allow close integration with existing scientific initiatives and relate different strategic areas which are funded through other agencies. It will bring together groups with their labs and infrastucture in an interdisciplinary environment for ultrafast X-ray science and we anticipate that this will greatly multiply scientific output. Being a medium-scale facility positioned between individual instruments and large-scale (inter)national facilities, allows the Ångström Laser to be placed in the middle of a university campus. It will thus provide a unique opportunity to link ultrafast X-ray science and accelerator and materials research to educational programs. The Ångstöm Laser, therefore, also represents an important "training hub" for young researchers in these science fields with wide-ranging and long-term impact from new approaches to materials discovery and characterization to the efficient use of large-scale facilities.

Acknowledgements

The work presented in this Conceptual Design Report was funded through the support of the FREIA Laboratory by the faculty of science and technology of Uppsala University. The following persons have contributed to the report:

Marcus Agåker[1], Johan Åkerman[2], Moyses Araujo[3], Martin Beye[4], Stefano Bonetti[5], Ute Cappel[6], Ruslan Chulkov[1], Saroj Dash[7], Martina Dell Angela[8], Anna Delin[9], Hermann Dürr[1], Marika Edoff[10], Mats Fahlman[11], Vitaliy Goryashko[1], Oscar Grånäs[1], Leif Hammarström[12], Tom Hase[13], Björgvin Hjörvarsson[1], Vassilios Kapaklis[1], Andreas Lindblad[1], Xianjie Liu[11], Marcus Lundberg[12], Edvin Lundgren[14], Anders Nilsson[5], Natalia Martin[10], Johannes Messinger[12], Akira Miyazaki[1], Ellen Moons[3], Venkata K. Muta[1], Markus Münzenberg[15], Anatoliy Opanasenko[16], Jinshan Pan[6], Gunnar Pálsson[1], Kevin Pepitone[1], Roger Ruber[1], Kai Rossnagel[4,17], Peter Salén[1], Gerd Schönhense[18], Vishal Shokeen[1], Johan Söderström[1], Yasmine Sassa[19], Hugo Strand[20], Magnus Skoglundh[21], Jacinto Sá[13], Zoltan Tibai[22], Oscar Tjernberg[9], Claudio Verdozzi[23], Jonas Weissenrieder[9], Philippe Wernet[1], Alexander Yaroslavtsev[1]

1 Department of Physics and Astronomy, Uppsala University
2 Department of of Physics, Göteborg University
3 Department of Engineering and Physics, Karlstad University
4 Deutsches Elektronen-Synchrotron DESY, Germany
5 Department of Physics, Stockholm University
6 Department of Chemistry, KTH – Royal Institute of Technology
7 Department of Microtechnology and Nanoscience, Chalmers University
8 CNR –IOM SS 14 km 163.5 Trieste, Italy
9 Department of Applied Physics, KTH - Royal Institute of Technology
10 Department of Materials Science and Engineering, Uppsala University
11 Department of Science and Technology, Laboratory of Organic Electronics, Linköping University
12 Department of Chemistry – Ångström Laboratory, Uppsala University
13 Department of Physics, Warwick University, UK
14 Division of Synchrotron Radiation Research, Lund University
15 Department of of Physics, Greifswald University, Germany
16 KIPT, Ukraine
17 Institut für Experimentelle und Angewandte Physik, Christian-Albrechts-Universität zu Kiel, Germany
18 Department of Physics, Mainz University, Germany
19 Department of Physics, Chalmers University
20 School of Science and Technology, Örebro University
21 Competence Center for Catalysis, Chalmers University of Technology
22 Pecs University, Hungary
23 Department of Physics, Lund University

We acknowledge the members of the Ångström Laser CDR Scientific Advisory Committee: William Graves (Arizona State University), Simone Di Mitri (Elettra Sincrotrone Trieste and University of Trieste) and Laszlo Veisz (Umeå University).

Table of Contents

Introduction: Why the Ångström Laser in Sweden?

Sweden has a long tradition in X-ray spectroscopy and structural analysis resulting in a broad and strong scientific community that uses X-ray facilities such as the MAX IV synchrotron in Lund and the European X-ray Free Electron Laser (EU-XFEL) facility in Hamburg where Sweden is a major stakeholder. These facilities provide X-ray pulses with very different characteristics and for complementary scientific use cases. EU-XFEL and other XFELs (the Swedish SXL project among them) deliver femtosecond short X-ray flashes at moderately low repetition rates but very high pulse intensities (red shaded area in Fig. 1.1).

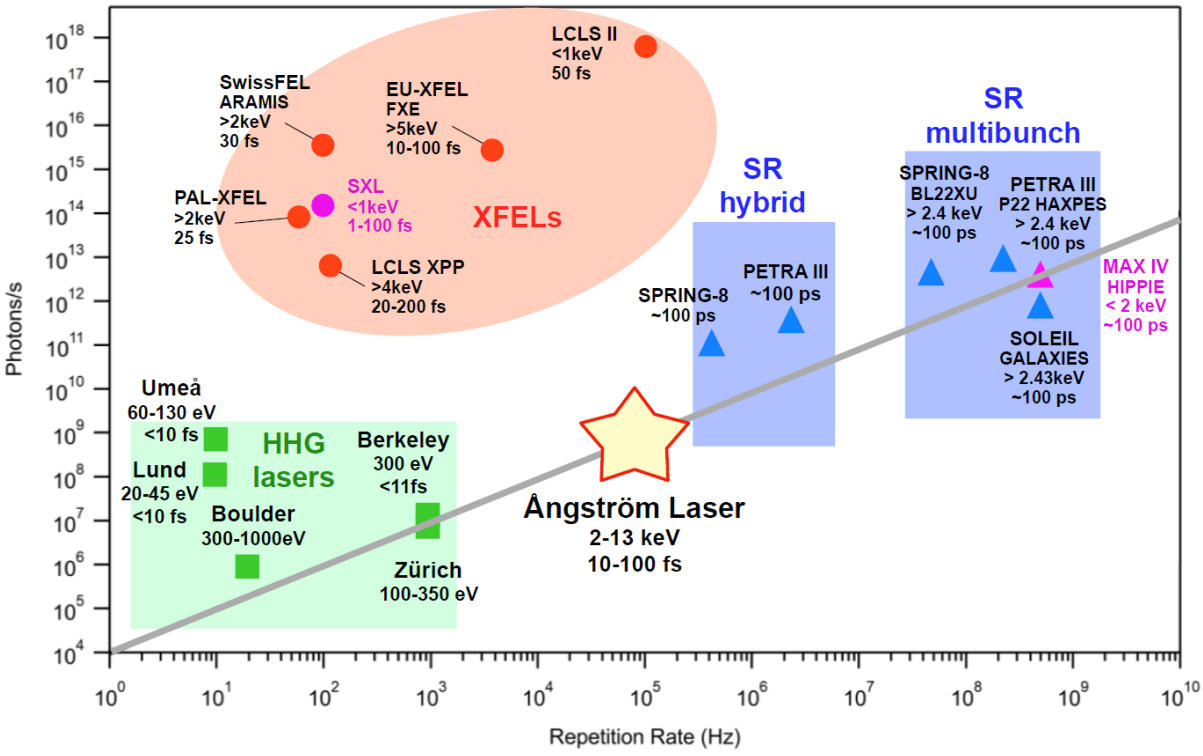

Figure 1.1: Pulsed X-ray facilities around the world with the MAX IV synchrotron and the SXL soft X-ray free electron laser project in Sweden. Also shown are high-harmonic generation (HHG) laser experiments in Boulder [1], Berkeley [2], Umeå [3], Zürich [4] and Lund [5]. Note that high-repetition-rate operation at the LCLS-II in Stanford will be available only for soft X-rays prior to the high-energy upgrade of the LCLS-II. The grey line roughly indicates the space-charge limit, above which energy blurring of photoelectron lines limits information content in photoelectron spectroscopy experiments (at a given repetition rate the X-ray pulse energy and the related number of electrons ejected from the material are limited to a resulting X-ray flux corresponding maximally to the values on the grey line).

These X-ray pulses are typically used to capture singular events with very short temporal duration. The prime example is the so-called probe-before-destroy imaging of individual biological nanostructures. To enable such single-shot experiments (where each X-ray pulse can be regarded being a separate experiment) and to compensate for losses in average photon

flux by bunching X-ray photons in single pulses, XFELs typically provide very high X-ray pulse intensities (many orders of magnitude more intense compared to synchrotrons). MAX IV and other synchrotrons in contrast (blue shaded areas in Fig. 1.1) deliver much longer and much weaker X-ray pulses, roughly 100 ps long, but at much higher repetition rates than XFELs. Synchrotrons can hence very accurately probe equilibrium properties of matter with repetitive or steady-state experiments. Also shown in Fig. 1.1 are laboratory-based soft X-ray laser sources (green area in Fig. 1.1) with a pulse duration comparable to XFELs but at significantly reduced X-ray photon flux.

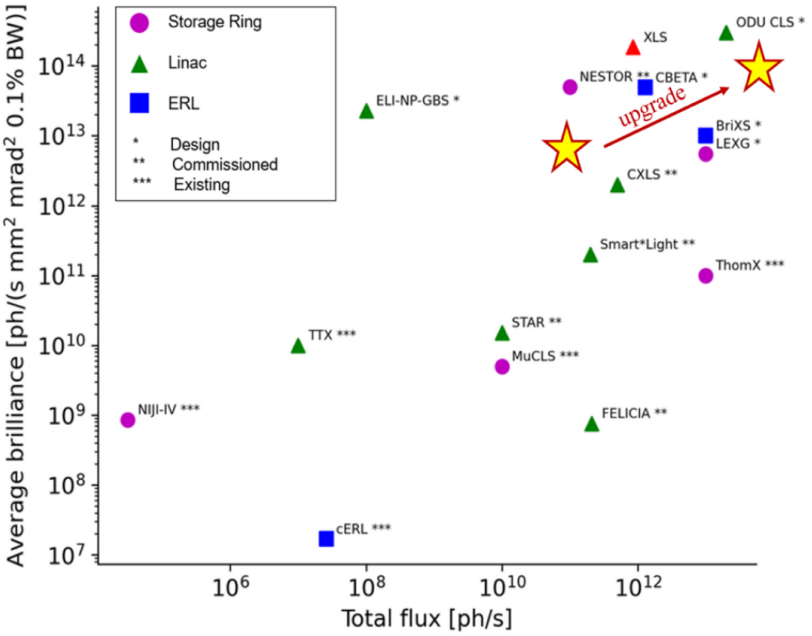

Figure 1.2: Overview of compact X-ray sources based on Inverse Compton Scattering (ICS) around the world in terms of average brilliance and flux. Existing, commissioned and designed inverse Compton sources are adopted from [6]. The baseline design and a future upgrade of the Ångström Laser are shown as red-rimmed yellow stars. Note that CXLS has generated first X-rays in Feb. 2023 and user operation is expected to commence later in 2023 [7].

The Ångström Laser represents a unique laboratory-based X-ray facility delivering femtosecond X-ray pulses with a unique combination of repetition rate and average X-ray flux as shown in Fig. 1.1 that makes it complementary to XFELs, synchrotrons and laser sources. With femtosecond short X-ray pulses like laser sources but at much higher repetition rate and photon energies, with an average flux like at a tender to hard X-ray dipole beamline of a synchrotron but at 1000 times shorter X-ray pulses, with femtosecond X-ray pulse durations and photon energies like at an XFEL but much lower pulse intensities, the Ångström Laser fills an important capability gap uniquely suited to address the described science cases in sustainability research. The average femtosecond X-ray flux is, in particular, sufficient to systematically probe dynamically evolving sample properties in dedicated sample environments with time-resolved measurements but it largely avoids damaging of the, often delicate, samples by too high X-ray pulse intensities. This results in a facility that is ideally suited for probing the dynamical properties of matter with timescales ranging over many decades. The Ångström Laser also resides in a parameter region (diagonal gray line in Fig. 1.1) where the X-ray flux is low enough to prevent the so-called space charge blurring of photoelectron spectra (when so many electrons are emitted from the sample by X-ray photoionization that they interact with each other and modify their kinetic energy, leading to the loss of the information content in the photoelectron spectrum). The Ångström laser will, in particular, enable to extend core-level photoemission, a technique prominently developed in Uppsala [8], into the time domain. We note that compa-

rable measurements will only be possible at the European XFEL in Hamburg (at approx. 10 kHz repetition rate) and the Linac Coherent Light Source (LCLS-II) in Stanford (at approx. 300 kHz repetition rate). However, there, X-ray energies only below 3 keV (Eu-XFEL) or around 1 keV (LCLS-II) are available. In addition, photoemission measurements at XFELs are only possible after severely attenuating the X-ray flux and only by sharing access with many more user groups. We envision the Ångström Laser to be a cost-effective alternative providing Swedish and collaborating international users with more access than what will be possible at XFELs for systematic studies in materials science.

The Ångström Laser is based on the interaction of a short electron bunch with an optical undulator created by a strong optical laser field, the so-called Inverse Compton Scattering (ICS) effect. Also within the landscape of compact X-ray sources based on ICS, the Ångström Laser is competitively positioned. Figure 1.2 shows the summary of existing, commissioned and designed inverse Compton sources around the world [6]. Existing sources are mainly based on circulating storage rings that are generating very high repetition rate X-ray pulses as, for instance, at the Munich Compact Light Source (MuCLS) where applications are largely dedicated to phase-contrast imaging of biological samples [9]. Imaging applications are also of interest for linear accelerator based inverse Compton sources such as SmartLight at Eindhoven Technical University [10] and CXLS at Arizona State University [11]. Both sources are in their commissioning phases. CXLS has generated first X-rays in Feb. 2023 and user operation is expected to commence later in 2023 [7]. The Ångström Laser in its baseline configuration and future upgrade to coherent lasing is depicted by the red-rimmed yellow stars. To assess the future impact of the Ångström Laser, it is interesting to note that its scientific applications outlined in chapter 2 encompass and significantly exceed those of the BESSY II FemtoSpeX facility, a synchrotron-based single-beamline source of soft X-ray pulses [12]. Although the X-ray flux of FemtoSpeX is about 2-3 orders of magnitude smaller than that anticipated for the Ångström Laser, due to technical limitations of the repetition rate, it occupies a unique niche for studying ultrafast processes in magnetic and strongly correlated electron materials. This has led to a significant number of high-profile scientific publications since FemtoSpeX started operation in 2007 [13] until today. We anticipate a similar opportunity for the Ångström Laser in the seven scientific areas described below.

Figure 1.3 gives an overview over some intrinsic timescales on which fundamental processes in materials science, chemistry and biology occur. The femtosecond (fs) pulse duration and microsecond (µs) pulse separation of the Ångström Laser will allow us to capture the spectroscopic fingerprints of these processes as they occur in real time started by a trigger event such as an optical laser, magnetic or electric field pulses.

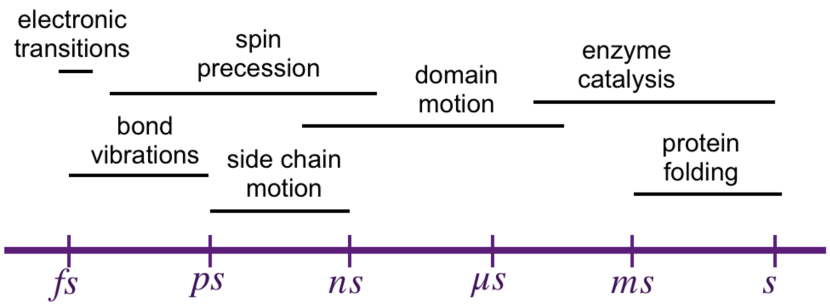

Figure 1.3: Dynamical processes in matter versus their intrinsic timescales. With its femtosecond X-rays and high repetition rate, the Ångström Laser will enable time-resolved X-ray experiments addressing the whole range of processes from the effects of local electronic transitions to collective motions in materials such as in those driving domain-wall motion and chemical kinetics in catalysis.

This document is organized as follows:

In chapter 2 we describe the science drivers and extract the benchmark parameters for the Ångström Laser design. Special emphasis is given to scientific grand challenges as they occur in materials science serving a sustainable world.

Chapter 3 is devoted to the technical description of the Ångström Laser. This includes the electron accelerator, X-ray generation and transport and experimental end stations. This chapter also describes the conditions enabling timing on the femtosecond timescale, layout of the Ångström Laser and upgrade possibilities.

Chapter 4 describes the budget and the timeline for building and commissioning of the Ångström Laser. It also describes the envisioned operation conditions and user access.

Science drivers for the Ångström Laser

While conventional synchrotron, electron and neutron sources have provided us with complementary views of atomic structures and electronic properties, their static descriptions are lacking access to the intrinsic timescales of fundamental processes. Short flashes of X-ray light gives access to these time scales and their availability is currently revolutionizing the way we look at and think of matter and materials. With a duration in the range of femtoseconds, such X-ray flashes make visible how atoms and electrons move as a material is transformed. This new capability offers unprecedented opportunities in observing, understanding and controlling materials and their function in a number of disciplines. Combining X-ray wavelengths down to the Å regime with femtosecond pulse durations and microsecond pulse spacings enables new ways of characterizing geometric and electronic structures of matter on the time scales of nuclear motion and with atomic spatial resolution, specificity to selected elements, chemical sites and molecular orbitals. Based on completely new experimental observables, this will enable the rational design of better and more sustainable materials in a way that has not been imaginable before the advent of femtosecond X-ray sources. Building on the strengths at Uppsala University and in Sweden, the Ångström Laser will offer a suite of new experimental end stations to address important related materials science questions in fields ranging from chemistry to catalysis and quantum materials science.

The following science drivers and their relationship to the interested user groups have been identified at a workshop on August 31, 2022 at Uppsala University (workshop contributions are accessible on https://indico.uu.se/event/1131, password “Alaser”). The unique materials characterization aspect of the Ångström Laser for probing fundamental processes on their intrinsic length- and timescales will directly link to their theoretical modeling. Continued access to this novel tool will enable new ways to explore and optimize performance, properties, structure, synthesis and design of materials and devices. This is expected to create new opportunities for all areas ranging from materials discovery to energy conversion and efficiency with direct impact on replacing problematic materials components and preserving our environment. The following topics will be discussed further below with special emphasis on materials science for a sustainable world:

1. Heterogeneous Catalysis: Creating a sustainable chemical industry
2. Molecular catalysis: Converting solar into chemical energy
3. Operando processes in photovoltaic materials
4. Understanding the time-resolved charge transfer in electrochemical processes
5. Materials for hydrogen storage
6. Energy efficient control of quantum materials properties
7. Towards energy-efficient information technology with topological materials

2.1 Heterogeneous Catalysis: Creating a sustainable chemical industry

Anders Nilsson[1], Edvin Lundgren[2], Magnus Skoglundh[3], Jacinto Sá[4], Andreas Lindblad[5]

[1]Division of Chemical Physics, Department of Physics, Stockholm University
[2]Division of Synchrotron Radiation Research, Lund University
[3]Competence Center for Catalysis, Chalmers University of Technology
[4]Department of Chemistry – Ångström Laboratory, Uppsala University
[5]Department of Physics and Astronomy, Uppsala University

Synopsis: *The world is facing a major challenge in converting the chemical industry from fossil source dependence and such a transformation will require new catalytic processes. It will be essential to monitor reaction intermediates on the surface of catalysts that often are transient, existing on extremely short time scales allowing for a deep understanding of the reaction mechanism. Furthermore, the reaction can also cause restructuring with changes of the chemical composition of the catalyst material. The Ångström Laser can provide an extraordinary opportunity to probe surface catalysis using pump-probe techniques based on X-ray photoelectron spectroscopy that are developed to operate at elevated pressures to match real reaction conditions.*

There are many base chemicals of importance for the catalytic production of fertilizers, plastics, detergents, pharmaceuticals and fuels. Currently, the feedstock for the chemical industry is entirely based on fossil sources with an emittance of 8% of the worlds footprint of greenhouse gases (not including when fuel is being burned). For instance, the annual production of the essential chemicals methanol and ammonia are both more than 100 million tons. Furthermore, methanol also has the potential to become a future energy carrier that can be converted to aviation fuel. There is an urgency to transform the chemical industry away from fossil sources and towards basing it on captured CO_2 and H_2 from water electrolysis [1]. A future green transformation of the chemical industry, similar to the one with green steel, where wind or solar energy drives electrolytic cells is therefore a possibility, see Fig. 2.1. In particular Sweden can be well equipped with new industries where large wind farms are located.

Catalysts are at the heart of these transformation currently based on fossil resources into products for use in everyday life. Naturally the catalysts in use today have been developed over a century with fossil resources in mind. The hydrogen pressure from electrolysis cells, however, are on the scale of ambient conditions (1 bar, 300 K). Thus, a paradigm change in the production of the reactants also necessitates a similar transformation of the catalyst. Consequently, theoreticians and experimentalists are now developing schemes that obtain catalysts in hitherto unexplored regimes, ideally matching the output of the upstream processes. This effort needs to be met with studies of the chemical state of the catalyst material and the reaction intermediates during reaction conditions in order to give feedback for the catalyst development [2]. It is essential that we obtain a fundamental understanding of the behavior of important intermediates on a timescale that is much shorter than the individual lifetimes of the intermediates on the surface of the catalyst in order to capture their transient behavior. Femtosecond (fs) time-resolved electronic structure changes in the atomic or molecular structure of the intermediates will not only provide important information on the electron driven dynamics and the overall activity and selectivity on an ultrafast timescale but will also address the long-time scale dynamic stability of the catalytic bulk material under various conditions such as different temperatures, pressures and reactant composition.

The surface chemical reactions in catalysis proceed through several elementary reaction

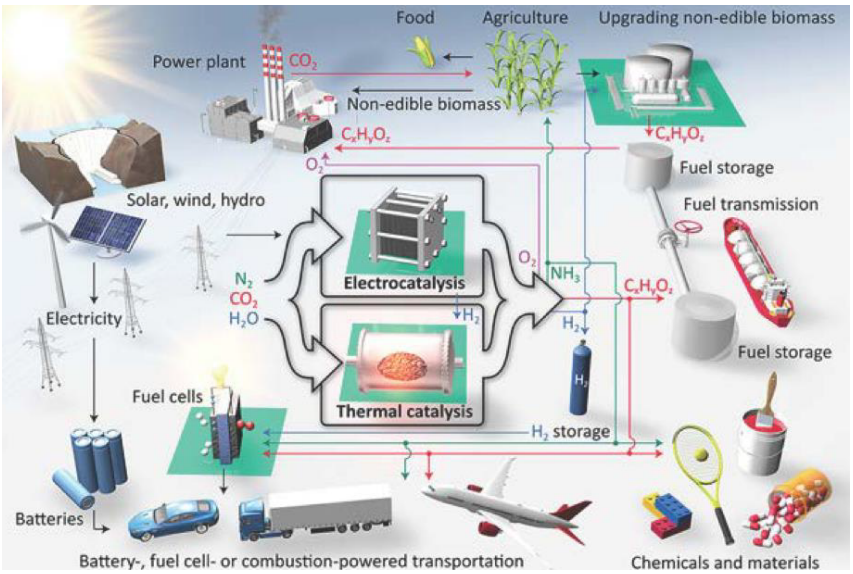

Figure 2.1: Illustration of a sustainable energy system to produce base chemicals for the industry and transportation fuel based on catalysis. Key processes are electrochemical water splitting and thermal and electrochemical CO_2 and N_2 reduction—graphics courtesy of Jakob Kibsgaard, DTU [1].

steps as shown schematically in Fig. 2.2 [3]. The kinetic rate of each step in the simple linear reaction is appropriately described using Arrhenius theory and generally the step in the process with the highest barrier and consequently the lowest rate defines the rate determining step and hence controls the turnover of a given reaction. Typically, catalysts are limited by their ability to effectively activate chemical bonds, i.e., when intermediates interact weakly with the surface, or they will bind intermediates too strongly and activity is limited by product desorption. The time scales involved in the elementary reaction steps involve atomic and molecular motions, which occurs somewhere between 100s fs - to a few picoseconds (ps). These processes are usually referred to as molecular dynamics in contrast to the overall reaction kinetics or stability and restructuring dynamics occurring on a much longer time scale. The outcome of most elementary steps gives rise to transient species which then react further to intermediate species [3]. Driving reactions in heterogeneous catalysis with an ultrashort (femtosecond) optical laser pulse provides a new window into these processes. By reaching these ultrashort time scales, it is possible to greatly increase the population of transient intermediates, facilitating their detection on an ultrafast time scale. The optical pumping of a metal creates a very hot electron distribution that lasts typically for 1-2 ps before decaying into phonons and creating a fully thermalized temperature similar to that in typical catalytic reactors and is well described by a two-temperature model. Both the hot electrons and the phonons could make or break various chemical bonds.

The Ångström Laser will allow for X-ray photoelectron spectroscopy (XPS), which provides high surface sensitivity combined with information on elemental compositions and the local chemical environment around a specific atomic site on surfaces. Technical advances have also extended this technique to ambient pressures (APXPS) close to one atmosphere [2] and the method has been widely used to characterize gas-solid surfaces at synchrotron light sources under the steady-state working condition of catalysts, as well as electronic structure changes in operating solid-oxide fuel cells, and other systems. With XPS at the Ångström Laser it will be possible to outline all the essential elementary steps of adsorbates and changes in the catalytic surface on 100 fs time scales that can provide full insight into the reaction mechanism and how catalytic material operates to achieve high activity and selectivity. Such insight will be

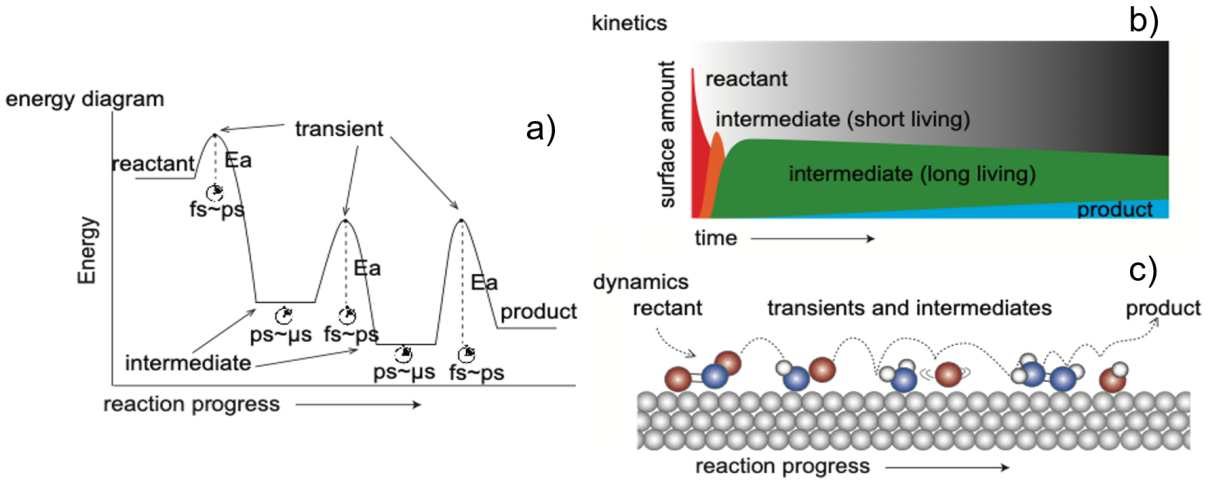

Figure 2.2: **(a)** Schematic energy reaction diagram indicating transition states and intermediates of different elementary reactions. **(b)** Illustration of the time development from reactant to product with both a transient short-lived and stable long-lived intermediate. **(c)** Picture of an example of molecular fragments during the various elementary steps.

fed into the design of new catalytic materials that can revolutionize the chemical industry into full sustainability.

2.2 Molecular catalysis: Converting solar into chemical energy

Leif Hammarström[1], Marcus Lundberg[1], Johannes Messinger[1,2], Philippe Wernet[3]

[1]Department of Chemistry – Ångström Laboratory, Uppsala University
[2]Center for Artificial Photosynthesis (CAP), Uppsala University
[3]Department of Physics and Astronomy, Uppsala University

Synopsis: *Making use of the energy from the sun to convert abundantly available molecules in a direct process into affordable and clean forms of energy carriers, liquid fuels or valuable compounds for industry forms the basis for the future of sustainable societies. By uncovering how atoms and electrons move in a chemical reaction, the Ångström Laser will let us discover new mechanisms in photo-driven molecular catalysis for the conversion of solar into chemical energy.*

Finding new ways of producing affordable and clean energy carriers, transforming CO_2 into valuable compounds, and making available new fuels for mobility and transport requires understanding and controlling chemical transformations. Using visible photons to control chemical transformations makes available the abundant energy from the sun [4, 5, 6, 7]. Important applications include photodriven water splitting, photochemical C-H bond activation, photocatalytic CO_2 reduction and photochemical hydrogen evolution (see Fig. 2.3).

The elementary processes in photo-driven molecular catalysis are notoriously difficult to capture as they occur on the atomic length and time scales of Ångströms and femtoseconds. The Ångström Laser will be a unique tool for an unprecedented characterization of molecular catalysts with specificity to selected elements, chemical sites and single orbitals. Owing to its femtosecond pulses, the Ångström Laser gives access to femtosecond photoexcited states and

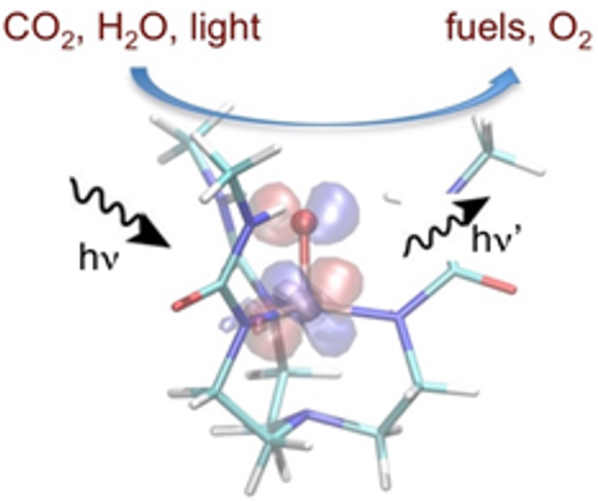

Figure 2.3: Seeing frontier molecular orbitals in solar fuel generation with the Ångström Laser.

enables determining how key reaction intermediates in catalytic reaction kinetics emerge from these. The femtosecond pulses will be essential, in addition, for probing sensitive samples before they are destroyed by the X-ray irradiation ("probe-before-destroy"). With its X-ray photon energy range from 2 to 13 keV, the Ångström Laser will cover the K-edges of first-row transition metals and the L-edges of second-row transition metals, thereby enabling time-resolved X-ray absorption spectroscopy from femtosecond dynamics to microsecond kinetics in chemical transformations with important homogeneous catalysts. In addition, by addressing the K-edges of important ligand elements such as S and P, time-resolved X-ray spectroscopy at the Ångström Laser will provide the full picture of how metal-ligand charge transfer and changes in coordination enable homogeneous catalysis. Seeing how atoms and electrons move in a reaction is the basis for developing new concepts for how to "engineer" or transform chemical bonds. Seeing the frontier-orbital interactions at the reactive sites in a molecular catalyst and in real time of the reaction will allow us to understand how to modulate reaction barriers and to make the overall process more efficient. The Ångström Laser will give us quantum-level explanations of chemical reactions and make us predict and discover new catalytic mechanisms. Understanding how to control chemical transformations with sunlight on the level of atoms and electrons will help making valuable molecules from abundant resources for new forms of fuels and clean chemicals for sustainable societies.

2.3 Operando processes in photovoltaic materials

Marika Edoff[1], Natalia Martin[1], Ute Cappel[2], Martina Dell Angela[3], Xianjie Liu[4], Mats Fahlman[4], Ellen Moons[5], Moyses Araujo[5], Oscar Grånäs[6]

[1]Department of Materials Science and Engineering, Solar Cell Technology, Uppsala University
[2]Division of Applied Physical Chemistry, Department of Chemistry, KTH – Royal Institute of Technology
[3]CNR –IOM SS 14 km 163.5 Trieste, Italy
[4]Department of Science and Technology, Laboratory of Organic Electronics, Linköping University
[5]Department of Engineering and Physics, Karlstad University
[6]Department of Physics and Astronomy, Uppsala University

Synopsis: *Photovoltaic solar energy conversion is an important aspect for a sustainable future. Development of technologies, which use abundant materials processed at low temperatures, is necessary for using solar energy conversion at its full potential. The Ångström Laser will open new ways to understand the initial ultrafast photo-induced charge separation across interfaces and subsequent charge transport within the materials. This will enable us to navigate the huge parameter space of photovoltaic materials families aimed at increased efficiency.*

Given the current energy and climate crisis, a clean and renewable energy source is crucial for a sustainable future [8, 9]. With one of the highest potentials among renewable sources, photovoltaic systems are among the cleanest sources of energy that directly convert solar energy into electricity. Several material systems have qualities that make them suitable for solar cell applications, where one divide is if the materials have an indirect bandgap (such as silicon) or a direct bandgap (such as perovskites, solar cell polymers, CdTe, CIGS, or GaAs). The individual materials and layers have to be combined with contacts as is exemplified in Fig. 2.4. An ideal contact should be selective and allow one charge type (electron or hole) to pass the contact, but repel the other type. Here we can distinguish between flat architectures, polymer blends or dye-sensitized solar cells, where the polymer blends and dye-sensitized solar cells are even more dependent on the selectivity of the contacts. Doping of materials will influence the depletion and capacitance in the devices and we see a difference between perovskite solar cells, which almost completely depleted absorbers, to silicon based solar cells, where only a small fraction of the absorber is depleted. Parasitic chemical reactions, or formation of electronically active defects (e.g. by lattice mismatch) at the interfaces may obstruct contact properties that should be ideal in theory. Better understanding of the light absorption and charge transfer dynamics as a function of depth and as a function of time in these materials is a key aspect in their efficiency optimization efforts.

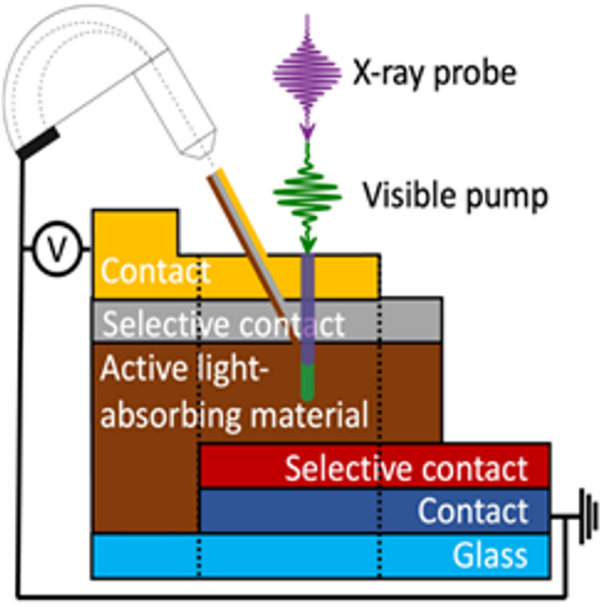

Figure 2.4: Operando TRPES measurements on a solar cell with different layers.

The Ångström Laser will enable several new time-resolved experiments to study these processes in detail for the different types of solar cells described above. Time-resolved photoelectron spectroscopy can be used to investigate charge transfer dynamics through photovoltage generation observed in core level shifts [10]. Using hard X-rays at the Ångström laser will allow for selective measurements of different layers at a solar cell interface through an optimal probing depth for thin interfaces (Fig. 2.4). This will enable the study of charge movement in the solar cell through different layers in time ranges spanning from femto- to microseconds.

Additionally, stacks of layers, or even complete devices can be measured in operando in such a set-up allowing to study how an external bias influences these processes. Interesting research questions could relate to dynamics, for instance, of bias-dependent (light or electronic bias) ion migration, charge transfer, or relaxation of excited states, which require different time resolutions. Possible challenges are beam damage, parasitic absorption in contact layers and sample roughness, that could influence the measurement results.

Recently, the efforts to optimize the selection of light-absorbing materials in order to mitigate power losses due to thermalization have brought to the scene down-conversion materials, which rely on the ability of certain materials to generate two, or more, low-energy excitons from the absorption of a single high-energy photon, thus potentially duplicating the charge carriers available for photocurrent generation [11]. Only few organic compounds, such as polyacenes and diradicaloids, have demonstrated down-conversion capabilities through singlet fission, i.e., the splitting of a singlet exciton into two triplet excitons, and many others are suggested [12]. However, the realization of efficient devices based on these materials calls for further fundamental requirements. In particular, the triplet excitons should be mobile enough to reach the active interface, and their separation and transfer should be favored over singlet exciton transfer by a proper energy level alignment, to take full advantage of the charge multiplication process. The charge separation can be tracked by measuring the surface photovoltage via photoelectron spectroscopy. The temporal information obtained by means of time-resolved photoelectron spectroscopy experiments at the Ångström laser will allow a fundamental description of the dynamics of the charge transfer states formed at the materials interfaces, with a crucial role to further improve the performances of organic photovoltaic devices. Furthermore, first-principles based atomistic modelling will be carried out to advance the fundamental understanding of photocurrent generation. The computational methodologies will span from electronic structure and excited state dynamics calculation to ion transport modelling.

2.4 Understanding the time-resolved charge transfer in electrochemical processes

Edvin Lundgren[1], Dragos Dancila[2], Jinshan Pan[3], Jonas Weissenrieder[4], Oscar Gråsäs[5]

[1]Division of Synchrotron Radiation Research, Lund University
[2]Department of Electrical Engineering, Solid State Electronics, Uppsala University
[3]Department of Chemistry, Division of Surface and Corrosion Science, KTH Royal Institute of Technology
[4]Department of Applied Physics, KTH - Royal Institute of Technology
[5]Department of Physics and Astronomy, Uppsala University

Synopsis: *Transition metal oxides are characterized by a complex interplay of nuclear, charge and spin degrees of freedom determining their functionality. A multitude of stable charge-states on the transition metal ion makes these materials ideal for anode materials in electrolysis cells or batteries, and as oxide films on industrial alloys in many energy applications where their properties are further affected by in-operando corrosion. The scarcity of ultrafast X-ray sources currently hampers systematic investigations of charge dynamics of oxide materials and limits our understanding of the ultrafast charge transfer processes in solid-electrolyte interactions. Such insight could turn out crucial for increased durability of materials important for a sustainable society, as well as the discovery of novel functionality.*

The stability/corrosion of anode electrodes at work is largely unknown. A major limitation is that for instance electrolysis for green hydrogen production faces high corrosion of the catalyst material at the anode, a process poorly understood and essential for establishing a

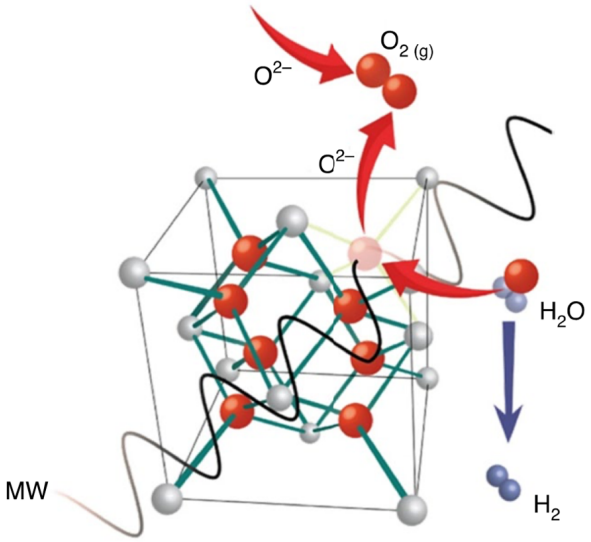

Figure 2.5: Schematics of H_2O reduction through extraction of one O atom by electromagnetic fields (MW) [13].

structure-function relationship [14]. The intermittent nature of wind and solar power energy sources causes difficulties which can be solved by energy storage technologies, to produce green hydrogen by splitting water using electrolysis, for later use in a fuel cell is an attractive solution. A fundamental understanding of the stability/corrosion/dissolution of the anode electrode would improve and facilitate hydrogen production. The development of more stable anodic material is needed for a sustainable society.

Similarly, passivity breakdown of industrial alloys such as stainless steels and Ni alloys can occur in corrosive environments, triggering localized corrosion such as pitting or rapid dissolution of the metal materials [15]. Corrosion of industrial alloys can cause dangerous and expensive damage to pipelines, bridges, vehicles, public buildings, water and wastewater systems, smart home and city appliances, electronics, batteries, sensors, and nanotechnologies [16]. A special form of corrosion, hydrogen embrittlement, of metals in infrastructures, especially hydrogen energy infrastructure, can lead to catastrophic material failure with serious consequences, even the loss of human life [17]. The stability of the passive oxide film, similar to the anodic dissolution process of the electrode, is also governed by the change of the metal oxidation state. Whereas hydrogen embrittlement involves cathodic reduction of the oxides. The lack of understanding of the corrosion initiation prevents mechanistic explanations of the observations regarding the stability and breakdown of passive films [18].

An example for new opportunities offered by time-domain studies with the Ångström Laser is illustrated in Fig. 2.5. Microwave fields were found to enhance H_2 production from water by extracting in first instance O^{2-} ions out of the Gd-doped ceria oxide anode, in a reduction process of the oxide material. This process creates oxygen vacancies, which leads to an increase in charge carriers and associated electrical conductivity; second, the activated material is re-oxidized as it spontaneously reacts with water at elevated temperature to form hydrogen. The principle is quite general and can be applied in many reactions to directly produce different molecular energy carriers, for example, in converting water and CO_2 into syngas, which can in turn be transformed into hydrocarbons.

Understanding the process dynamics and the underlying mechanisms would lead to the optimization of these reactions and this could be achieved using the Ångström laser. It is not entirely clear at the moment at what time-scales these reactions occur, if driving field stimu-

lated bond stretching vibrations lead to bond breaking and to what degree the fundamental interactions in the oxide material are involved.

The Ångström Laser will enable observation of time-resolved oxidation state transformations and their intermediates in operando. Electronic transitions (electronic-structure changes) in an electrolysis reaction as the electrode dissolves/corrodes can be observed in real time induced by external stimuli opening the way to probe the fundamental electronic nature of an electrolyzer induced chemical phase transformation. Combined with theory, the information would provide us with a detailed model of the process of corrosion/dissolution necessary for an atomistic design of future electrodes and advanced alloys resistant to corrosion including hydrogen embrittlement.

2.5 Materials for hydrogen storage

Gunnar Pálsson[1], Jinshan Pan[2], Björgvin Hjörvarsson[1]

[1]Department of Physics and Astronomy, Uppsala University
[2]Division of surface and corrosion science, KTH – Royal Institute of Technology

Synopsis: *The future use of hydrogen as a sustainable energy source necessitates innovative scientific breakthroughs in carbon-neutral hydrogen production, safe delivery and storage. The Ångström Laser will enable new ways to probe the interaction and dynamics of hydrogen with materials. This can enable novel chemical and materials synthesis, further our understanding of hydrogen interactions with molecules and materials and facilitate tracking and understanding of reaction pathways.*

The interest for the use of hydrogen as an energy carrier has increased dramatically lately. Not only can hydrogen provide a carbon neutral link in future energy systems [19], it can also be one of the cornerstones of storing energy from renewable sources, solving the emerging clean energy crisis. The transition towards hydrogen-based energy carriers is being accelerated by the plans of using hydrogen as an agent for removing oxygen in iron production. The replacement of carbon by hydrogen in steel production will lower the carbon footprint of Sweden dramatically. Hence, to meet both unforeseen and foreseen challenges we need to develop scientific and engineering expertise within the area of hydrogen in materials and hydrogen-based processes.

Here we highlight for the case of H diffusion in materials how the Ångström Laser will provide unprecedented new insight by directly detecting the diffusion process in the time domain. Calculations of H in Nb predict temperature dependent hopping timescales ranging from several 100 fs to several 10 ps (see Fig. 2.6 and [20]). This can be triggered by a fs laser pulse that transiently heats the host lattice and induces the H diffusion. X-ray diffraction from the Ångström Laser will be able to probe this by detecting characteristic changes in the hydrogen-induced lattice distortions via diffuse X-ray scattering [21]. The Ångström Laser will enable to probe the influence of H on lattice vibrations (phonons) that often lead to temporal oscillations in the time-resolved X-ray scattering signal. The experiments will provide completely new insight into the transport of hydrogen in metals, especially the interplay of the hydrogen interstitial and the local strain field. X-ray diffraction experiments can be extended to probe static and dynamic lattice changes, providing information related to imperfections (defects, surface, cracks etc.) as well as phase transformations [22, 23, 24].

In addition, H-induced changes of the valence electronic structure such as metal-insulator transitions can very sensitively be detected as electronic core level shifts of the constituting host material elements. Time-domain core-level photoemission measurements enabled by the

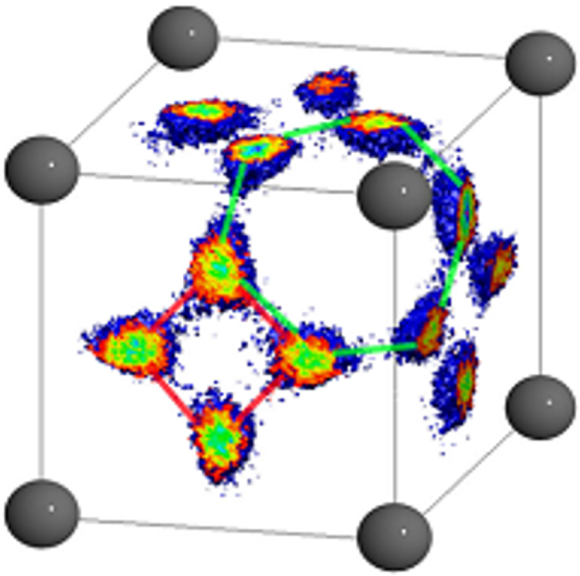

Figure 2.6: Positions and energy barriers of H in Nb [20].

Ångström Laser will for the first time be able to reveal dynamical changes/fluctuations of the electronic structure with H hopping.

2.6 Energy efficient control of quantum materials properties

Oscar Tjernberg[1], Jonas Weissenrieder[1], Anna Delin[1], Saroj Dash[2], Kai Rossnagel[3], Hugo Strand[4], Stefano Bonetti[5], Venkata Muta[6]

[1]Department of Applied Physics, KTH - Royal Institute of Technology
[2]Department of Microtechnology and Nanoscience, Chalmers University
[3]Institut für Experimentelle und Angewandte Physik, Christian-Albrechts-Universität zu Kiel, Germany
[4]School of Science and Technology, Örebro University
[5]Department of Physics, Stockholm University
[6]Department of Physics and Astronomy, Uppsala University

Synopsis: *The properties of what has come to be referred to as quantum materials and topological states, energy materials, materials with reduced dimensionality, superconductivity, ferroelectricity and magnetism can be manipulated with ultrashort laser pulses. Revealing the femtosecond dynamics of materials' properties with ultrashort X-ray pulses gives access to how elementary particles, charges, spins, phonons or magnons are coupled on their intrinsic time scales. This will allow controlling the properties of materials on femtosecond time scales. It will help develop new devices for ultrafast information technology as well as understanding novel magnetic functionality in energy conversion.*

Quantum materials display fascinating new physical properties due to the quantum mechanical nature of their electronic and atomic constituents. Novel ways to drive and manipulate these quantum effects are expected to result in transformative technological opportunities ranging from nearly dissipation free power management over novel forms of supercomputing to ultrasensitive sensors [25]. The ability to drive quantum materials into strongly non-equilibrium conditions open up radically new pathways for controlling the quantum mechanical coupling

between electron, spin and lattice degrees of freedom that determines the material's functionality. Possibilities range from stabilizing novel metastable so-called "hidden" states that have no equivalent in thermal equilibrium science [26] over possible control of topology via excitation of collective modes [27] to ultimately inducing superconductivity via external stimuli [28].

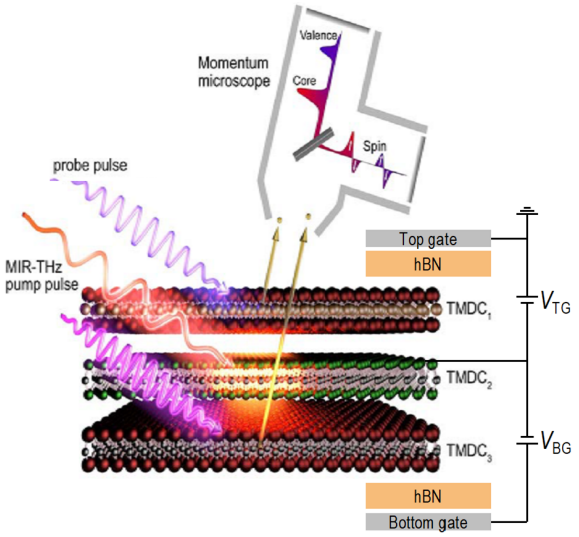

Figure 2.7: Seeing functionalized layers of quantum materials with a momentum microscope at the Ångström Laser.

The Ångström Laser will open up new ways to probe functional properties of quantum materials under operando conditions. Fig. 2.7 illustrates this for transition -metal dichalcogenide layers embedded in a transistor setup. Pump – probe studies can then reveal excited-state properties and non-equilibrium pathways while, for instance, electrical charges are injected into the layers or electrical bias voltages are applied. Photoemission spectroscopy using a so-called momentum microscope has become a unique technique to detect electronic structure changes of valence and core levels with spatial and temporal resolution [29, 30]. In addition, the diffraction of core-level photoelectrons from surrounding atoms is a sensitive tool to detect the atomic structure dynamics in the same experimental setup.

2.7 Towards energy-efficient information technology with topological materials

Yasmine Sassa[1], Saroj Dash[2], Johan Åkerman[3], Claudio Verdozzi[4], Markus Münzenberg[5], Venkata Muta[6]

[1]Department of Physics, Chalmers University
[2]Department of Microtechnology and Nanoscience, Chalmers University
[3]Department of of Physics, Göteborg University
[4]Department of of Physics, Lund University
[5]Department of of Physics, Greifswald University, Germany
[6]Department of Physics and Astronomy, Uppsala University

Synopsis: *The intrinsic coupling of electron spin and charge propagation in topological materials gives rise to phenomena of direct relevance to information technology application such as dissipationless transport and the formation of topologically protected nanoscale spin textures. X-ray pulses from the Ångström Laser will enable imaging of these processes under in-operando conditions required for future sustainable applications.*

The global electricity usage for communication technology continues to increase steadily and the International Energy Agency predicts that global electricity demand will triple between 2000 and 2040 approaching 40000 TWh. In microelectronics power and heat dissipation continues to grow threatening an energy crisis in computation. Novel energy-efficient architectures for storing, transmitting and processing data are required. The use of the electron spin has closely linked basic science discoveries to applications in information technology. Examples range from the discovery of giant magneto-resistance (Physics Nobel Prize 2007) to quantum computing.

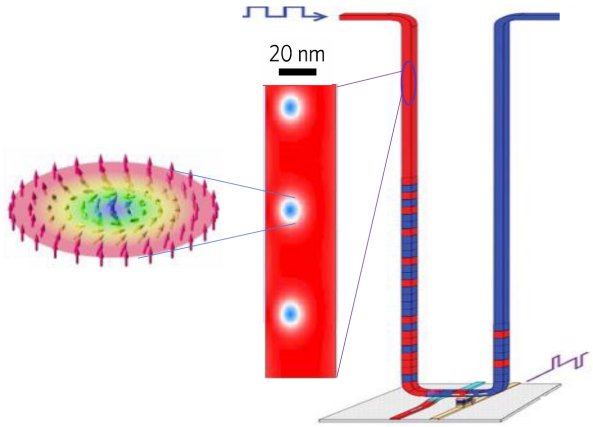

Figure 2.8: Illustration how the use of skyrmions, topologically protected spin nanostructures, [31] could revolutionize racetrack memory devices [32].

The dynamics of topologically protected magnetic spin textures, e.g., skyrmions, is of high current interest not only for fundamental science but also in applications for data storage and processing (see Fig. 2.8). Spin textures can be generated by spin-wave condensation out of the laser-excited, non-equilibrium state [33, 34]. The Ångström Laser will enable us to develop the fundamental understanding of the non-equilibrium pathways leading to skyrmion formation. Of particular interest is the question how topological spin textures emerge from condensating spin waves into solitons and when fluctuations of the topological charge are frozen out. Experimentally we will investigate various excitation mechanisms (light and electric current pulses) interacting with nanostructured materials to assure that skyrmion nucleation occurs repetitively at the same position. The momentum microscopy at the Ångström Laser will then enable the stroboscopic imaging of the non-equilibrium birth and the subsequent skyrmion motion depending on materials parameters. Theory will provide an understanding of their formation and interaction via atomistic spin dynamics calculations, as well as multi-scale (atomistic-continuum) dynamics. Furthermore, with theoretical modeling inclusive of both localized spins and itinerant electrons on equal footing it will be possible, by looking at the electron dynamics (e.g. via light-induced currents or time resolved photoelectron spectra, to electronically fingerprint skyrmions and possibly achieve new or improved ways to manipulate them. Such insight will be fed into the design of new, highly efficient data information technology devices that can transform communication technology into full sustainability.

2.8 Summary of required X-ray beam parameters and end stations

The science drivers described above require probing the temporal evolution (from femto- to microseconds) of the electronic and atomic structure of functional materials in various sample environments ranging from ultra-high vacuum over ambient pressure to liquids. They also utilize

external stimuli to trigger the processes to be studied via fs optical laser pulses (over a broad photon energy range from the far infra-red to the optical spectral range), electric or magnetic field pulses or even under microwave exposure. Experimental end stations therefore need to be flexible enough to contain the required sample environments and provide sample access for the external trigger signals.

Table 2.1 attempts to match the individual science drivers onto experimental techniques and end stations. We anticipate that the initial commissioning of the Ångström Laser will be mainly performed using an existing photoemission end station without any of the high-pressure characteristics or spatial resolution capabilities described in section 3.7. This end station is based on the Scienta ARTOF spectrometer which will be re-fitted with a high-kinetic electron energy lens system. In addition, we will work with Gerd Schönhense, who developed momentum microscopy, to have a momentum microscope available during commissioning of the Ångström Laser (see letters of support).

Table 2.1: Projected use of experimental techniques and end stations for the individual science drivers.

Science Driver	**High-Pressure Photoemission**	**Momentum Microscope**	**Transient Absorption**	**(resonant) XRD**	**ARTOF Photoemission**
Heterogeneous catalysis	> 50%	< 50%			< 50%
Molecular catalysis: Converting solar into chemical energy	< 50%		> 50%		
Operando processes in photovoltaic materials	< 50%	< 50%			< 50%
Charge transfer in electrochemical processes	< 50%		< 50%	< 50%	< 50%
Materials for hydrogen storage	< 50%	< 50%		> 50%	< 50%
Energy efficient control of quantum materials properties		> 50%		< 50%	< 50%
Energy-efficient computing with topological materials		> 50%		< 50%	< 50%

The workhorse technique to probe the electronic structure evolution is photoelectron spectroscopy using in particular core level electrons for an element specific monitor of the chemical and magnetic state of the atom. The high kinetic energy of the photoelectrons is necessary in order to provide bulk sensitivity e.g. in photovoltaic devices or enable the electrons to pass through a liquid layer or a gas environment under ambient pressure for the case of catalysis. Investigations on quantum materials on the other hand require ultrahigh vacuum conditions combined with nanometer spatial resolution and depth sensitivity to access buried interfaces.

In chapter 3 we describe two separate photoemission end stations that fulfill these requirements. During the science case workshop it was identified from existing measurements that photoelectron spectroscopy requires an X-ray flux of typically 10^8-10^9 photons per second in a 0.02% bandwidth at X-ray photon energies between 2-8 keV. For these conditions 10^2-10^3 photons per pulse at the Ångström Laser (see Table 1) typically lead to 0.1-1 photoelectrons e.g. for 2p core-levels of 3d transition metals. The 100 kHz repetition rate will thus enable 10^4-10^5 photoelectrons/s to be detected in a large solid angle (see section 3.7 on end stations). Time delay scans with typically 100 delay steps can therefore be obtained with good statistics in a matter of minutes. A dedicated end station for High-Pressure Photoelectron Spectroscopy is being proposed by A. Nilsson and his designated successor M. Beye through Stockholm University. A momentum microscope photoemission end station is being proposed by O. Tjernberg through KTH.

Transient absorption experiments are identified to investigate 4d-metal catalysts such as Rh, Ru, Mo and Pd for solar-fuel production. Pump-probe experiments in transmission mode will provide local charge and spin dynamics with fs time resolution. This type of investigation adds to the understanding of quantum level photocatalysis and enables new predictions of (photo)catalytic function. Extrapolating from current measurements a broadband X-ray flux of 10^9 photons/s (see Table 1) will enable measuring a full data set of one or two samples within one week (estimate based on beam for 12 h per day). A transient absorption end station can be placed in the broadband beamline (see section 3.5.1).

X-ray diffraction experiments are identified in science case 4-7. Hydrogen diffusion in materials can be studied, which is of relevance for energy storage and battery development. However, many of the other science cases have also the need for structural sample characterization with X-ray diffraction. While time-resolved X-ray diffraction can already be done by fs laser driven plasma sources, the Ångström Laser will offer the distinct advantage of being able to tune the X-ray energy into absorption edges for element-specific resonant X-ray scattering. For crystalline samples this is not a very flux hungry technique and the Ångström Laser parameters given in Table 1 are completely sufficient. However, the diffuse X-ray scattering from lattice strain, for instance, induced by hydrogen loading needs to be considered separately. For the case of H in Nb [21] such measurements could be performed with a rotating anode X-ray source with a typical flux of $\sim 10^7$ photons/s in about 1% energy bandwidth. This is easily achievable with fs pulse durations at the Ångström Laser (see Table 1).

Technical description of the Ångström Laser

3.1 Overview of the compact femtosecond X-ray source

In conventional X-ray facilities (synchrotrons and XFELs) X-ray pulses are generated from electron bunches in permanent-magnet undulators up to 100 m in length. Here we propose to replace these permanent-magnet undulators by the significantly more compact "optical undulator" of an intense optical laser field. In such a so-called inverse Compton source, laser pulses collide head on with electron bunches at relativistic speeds. The strong laser field acts very much like the magnetic field of a conventional undulator wiggling the electrons back and forth emitting X-rays in the process. This is a well-known principle that is being used in various places worldwide to generate X-rays. Now, here in Uppsala, with the existing unique instrumentation and experience combined with the now available new high-power commercial laser systems, we want to realize an optical undulator for a new ultrafast X-ray source in Sweden. The synergy of this optical undulator with a high repetition rate superconducting accelerator will make available the Ångström Laser – a femtosecond X-ray source with, due to the dramatically increased repetition rate, radically increased photon flux compared to existing inverse Compton sources. Our simulations indicate for the Ångström Laser baseline design a flux ranging from 10^9 photons/s in a 1% energy bandwidth (for use of polychromatic X-ray radiation) to 10^8 photons/s in a 0.02% energy bandwidth (for use of monochromatic X-ray radiation) at 2-8 keV X-ray energy and a 100 kHz repetition rate (see Table 1). Existing infrastructure at Uppsala University's FREIÅ Laboratory is essential for the innovative design of this X-ray source.

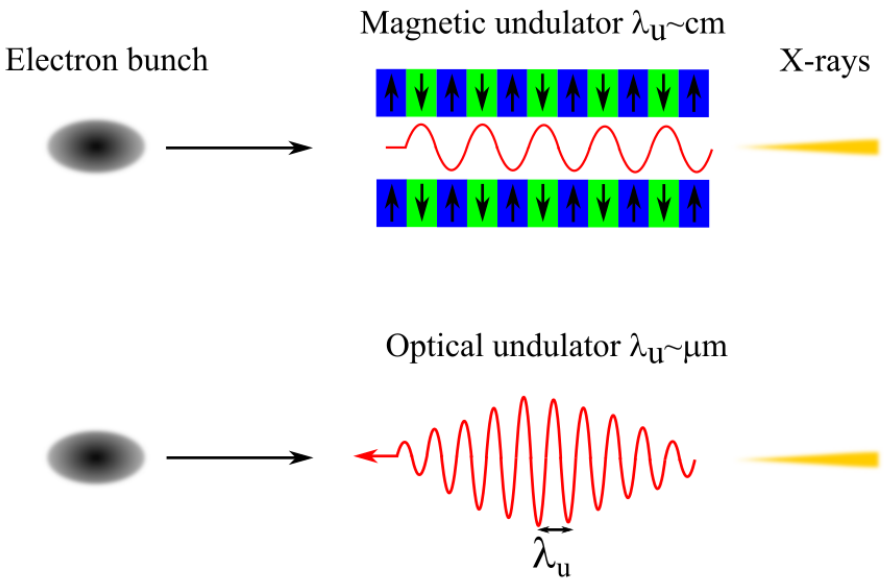

Figure 3.1: Comparison of the traditional permanent-magnet undulator (upper figure) and the optical one (bottom). The red waves symbolize the fields of the undulators with λ_u indicating the characteristic periods for the two types of undulators. The large difference in λ_u makes the optical undulator in an inverse Compton source so comparably short or compact.

Figure 3.1 illustrates the analogy between the two types of X-ray undulators. Since the laser-undulator period corresponds to the laser wavelength, much shorter electromagnetic field periods are accomplished compared with magnetic structures. This enables shorter undulators and a reduction of the required electron energy for producing X-rays, which permits shorter linear accelerators (linacs). Hence, the total size of the accelerator-based X-ray sources can be significantly reduced.

The Ångström Laser is based on scattering of mid-relativistic electron bunches on 1 µm-wavelength laser radiation. The tuning range of generated X-ray radiation is shown in Fig. 3.2 and covers the range of 2 to 8 keV as the electron beam energy is varied from 10 to 22 MeV. Production of X-ray photons with higher energies is planned via the use of the second (instead of first) harmonic of the laser driving the optical undulator.

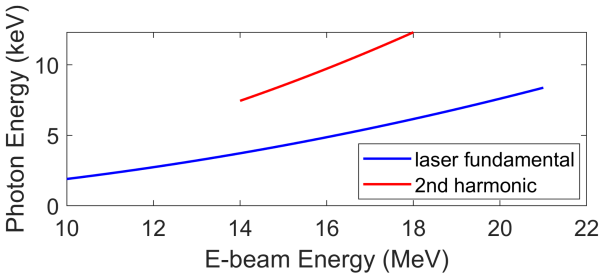

Figure 3.2: Tuning range of the Ångström Laser.

The Ångström Laser builds on several enabling technologies that recently became mature to be used in a user facility: (1) normal conducting very high frequency photocathode guns for the generation of high-brightness electron beams with ultra-low emittances, (2) superconducting (SC) cavities for efficient acceleration of high-repetition-rate beams, (3) high-repetition-rate and high-pulse-energy commercial optical/IR lasers with kW powers, and (4) novel end stations, such as ARTOF and momentum microscope (see section 3.7), for ultrasensitive X-ray and electron detection for analyzing the often subtle changes in the samples in question.

3.2 Linear accelerator

The linear accelerator comprises three units (see Fig. 3.3): (1) an injector for the generation of electron bunches with ultra-low emittances, (2) a superconducting accelerator for the acceleration and compression of electron bunches, and (3) a module for beam energy tuning and transverse focusing. The injector consists of an APEX-like normal conducting gun [1] followed by an ultracompact solenoid for beam collimation. A normal conducting booster immediately follows the gun and together they form a single mechanical structure. The TESLA SC cavity is at the heart of the accelerator. It brings the beam to a fixed energy of around 16 MeV (approximately in the middle of the tuning range). Simultaneously, strong bunch compression is realized in the SC cavity by means of initial deacceleration and ballistic bunching. The beam is then sent into the energy tuning module that decreases or increases the beam energy to generate X-rays at a desired photon energy (see Fig. 3.3). The last focusing element squeezes the beam size to the micron scale.

Key parameters of the electron bunch after each of the units are shown in Table 3.1. For a particular set of accelerator parameters, the evolution of the bunch parameters along the accelerator is depicted in Fig. 3.4. Beam dynamics simulations performed with the simulation code ASTRA [2] predict the RMS bunch radius and FWHM duration of 3.5 µm and 100 fs, respectively. The bunch energy is 16 MeV. To the best of our knowledge, such extreme compression of the bunch is one of the highest demonstrated in numerical simulations at the relatively low

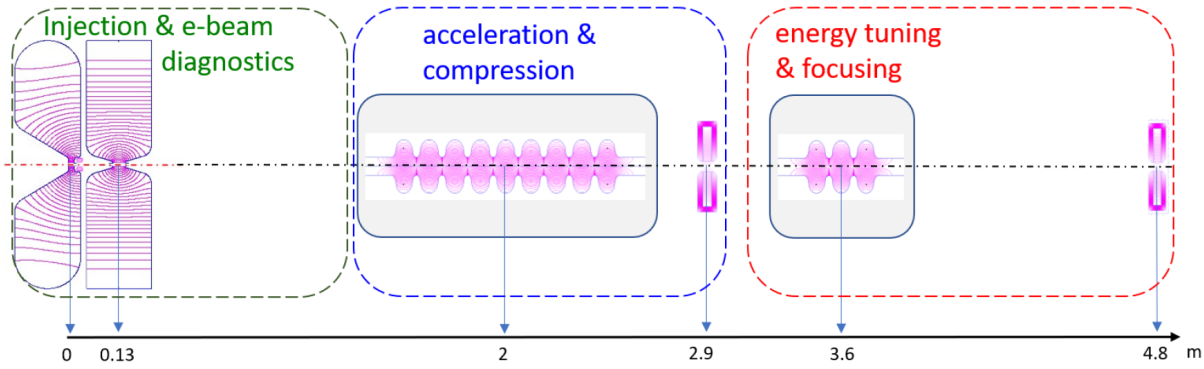

Figure 3.3: Accelerator layout with an APEX-like normal conducting injector gun followed by an ultracompact solenoid and a normal conducting booster. The TESLA cavity compresses the beam longitudinally and brings it to a fixed energy. The energy tuning module decreases or increases the beam energy to generate X-rays at a desired energy. A magnetic lens at the end focuses the beam. The distances of each unit from the electron source are given in m and the pink lines in the cavities represent electric RF field lines.

bunch energy used here. We note that in the example shown in Fig. 3.4, emittance compensation is not fully optimized and there is room for further emittance reduction.

Table 3.1: Electron beam parameters after key accelerator parts. **RMS** quantities are specified for all parameters except the bunch duration which is given as **FWHM**.

Parameter	**Injector**	**TESLA module**	**Tuning and focusing**
Energy	1 MeV	16 MeV	10-22 MeV
Energy spread	9.7 keV	30 keV	30-80 keV
x-beam size	240 µm	1000 µm	3-5 µm
z-beam size	770 µm	70 µm	50 µm
Duration	2.66 ps	0.23 ps	0.1-0.2 ps
x-emittance	65 nm	230 nm	100-200 nm
z-emittance	0.4 keV $\times$ mm	0.4 keV $\times$ mm	0.8-1 keV $\times$ mm

Our accelerator design relies on several solutions that are not common in the field of accelerators such as (1) operation of the RF gun in the blowout regime and (2) ballistic bunching inside the SC cavity. Therefore, a more detailed discussion of the accelerator operation is presented in the next subsections.

3.2.1 Radiofrequency gun

For the production of electron bunches at a high repetition rate, we decided to follow the success of the very-high-frequency photo-gun APEX developed at Lawrence Berkeley National Laboratory and employed in the LCLS-II project [3, 4]. But for our project we chose to change the gun cavity frequency to 325 MHz for two reasons: (1) to make the cavity more compact compared to lower frequency counterparts and (2) to have the gun frequency compatible with that of the TESLA cavity (1.3 GHz) for further beam acceleration and manipulation. In addition, the gun geometry was adjusted to balance the cavity impedance vs the flatness of the field profile. Figure 3.5 illustrates three cavity geometries with two geometries optimized for the maximum cavity impedance and the flatness of the field profile, respectively. The flatter field profile, the better the emittance. Finally, a compromised solution is employed. The cavity parameters for the three scenarios are summarized in Table 3.2. Further details on the gun

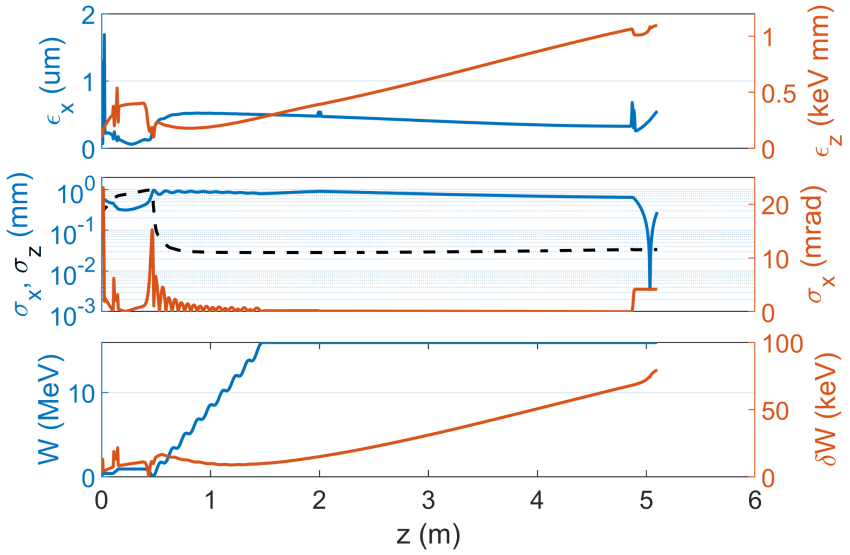

Figure 3.4: Evolution of the electron bunch parameters along the accelerator. At the position of the final focus at around 5 m, the bunch radius and duration attain values of 3.5 um RMS and 100 fs FWHM, respectively. The relative energy spread amounts to 0.5%.

cavity design can be found in [5].

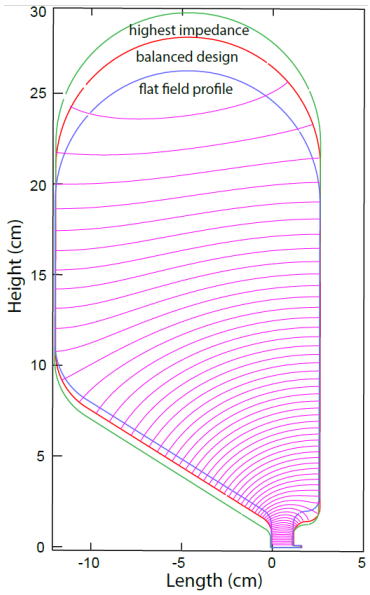

Figure 3.5: Geometry of the RF gun cavity. Three profiles represent the scenarios of the highest impedance (green), the flattest profile of the accelerating field (blue) and a balanced design (red).

The resulting gun design employs a peak accelerating field of 35 MV/m. The bunches are accelerated on-crest to an energy of 420 keV. Massive simulations have been performed to identify the optimum parameters for reaching the minimum emittance of an electron beam in the blow-out mode. The bunch parameters on the cathode for an optimal regime are reported in Table 3.3. Note that beam dynamics simulations were independently cross-checked using three different codes: ASTRA, GPT and RFtrack. The discrepancy between the results is less than 5% and in what follows only the results from ASTRA simulations are shown.

The emittance calculation results scanned over the initial laser spot size and duration are

Table 3.2: Cavity parameters for the scenarios described in the text.

Parameters	**Low power**	**Flat field**	**Balanced**	**APEX2**
Quality factor Q_0	44890	36600	41210	-
Shunt impedance, MΩ	8.7	6.6	7.8	-
Shunt impedance per unit length, MΩ/m	529.1	400.7	471.3	-
Peak-to-cathode field ratio E_{max}/E_{cat}	1.3	1.2	1.2	1.09
Electric field at the cathode, MV/m	35	35	35	34
Energy gain, keV	389	419	417	820
Power dissipation, kW	17.3	26.6	22.4	90.7
Max. power density on the wall, W/cm^2	13.7	23.5	18.6	32.1
Stored energy, J	0.42	0.48	0.45	-

Table 3.3: Optimal bunch parameters on the cathode. For an ellipsoidal bunch, the RMS size σ_x is related to the center-to-edge radius R as σ_x = R/$\sqrt{5}$.

Parameter	**Symbol**	**Value**	**Units**
Peak accelerating field	E_{acc}	35	MV/m
Emission phase	-	0	degrees
Charge	Q	16	pC
Energy	W	130	meV
Energy spread	δW	80	meV
RMS x-bunch size	σ_x	107	µm
RMS bunch duration	σ_t	30	fs
RMS x-beam divergence	$\sigma_x^{'}$	2.47	mrad
RMS thermal x-emittance	ε_x	44	nm

presented in Fig. 3.6. There is a clear minimum of the emittance for the initial bunch duration of 30 fs (shortest duration in the simulations) and the bunch radius of around 220 µm. The resulting lowest emittance for the 16 pC extracted bunch is 25% above the thermal level. In this optimum scenario, the longitudinal space-charge force (accounting for the image charge on the cathode) is around 35% of the accelerating field, which is an unexpectedly high ratio. The discovered regime allows generating bunches with the highest 6D brightness compared with the regime of flattop cylindrical bunches. Table 3.4 reports the beam parameters at the gun exit. Evolution of the bunch parameters along the gun and a normal conducting booster is depicted in Fig. 3.7. Further details on beam dynamics in the RF gun can be found in [6].

Table 3.4: Beam parameters in free space after the gun at 80 mm from the cathode.

Parameter	**Symbol**	**Value**	**Units**
Charge	Q	16	pC
Energy	W	420	keV
Correlated energy spread	δW	5.3	keV
RMS x-beam size	σ_x	2	mm
RMS z-beam size	σ_x	0.46	mm
RMS x-beam divergence	$\sigma_x^{'}$	24.4	mrad
RMS normalised x-emittance	ε_x	57	nm
RMS normalized z-emittance	ε_z	0.24	keV·mm
ratio of x and y emittances		0.99	

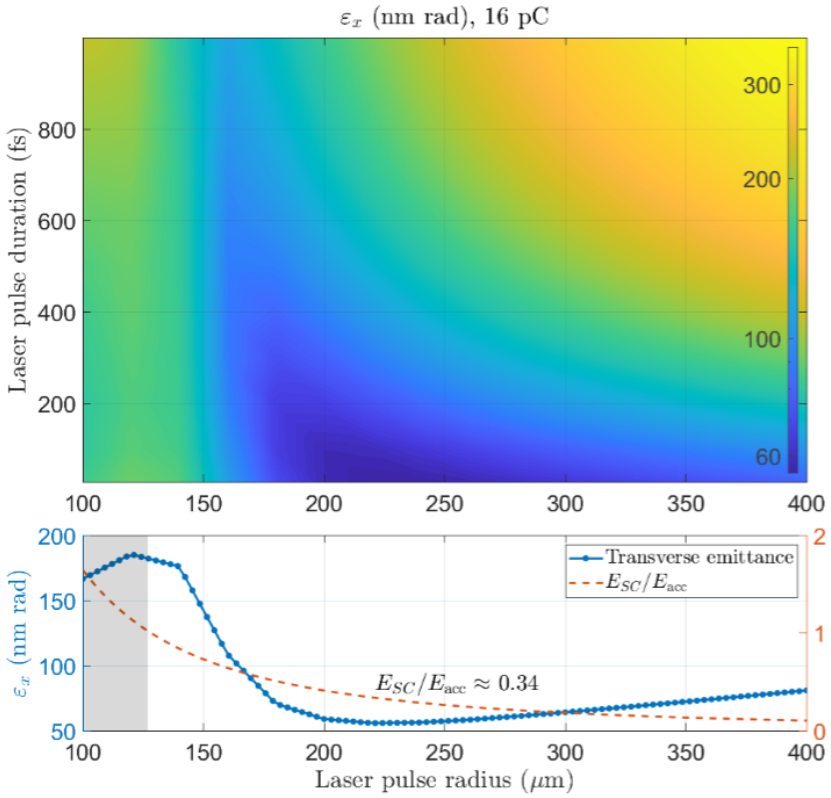

Figure 3.6: Upper plot: color map of emittance as a function of the initial RMS bunch duration (changes from 30 fs to 1 ps) and bunch radius R (note that R is the centre-to-edge distance; for an ellipsoidal bunch, σ_x = R/$\sqrt{5}$). Bottom plot: emittance (left ordinate axis) and E_{SC}/E_{acc} (right ordinate axis) as a function of R for the initial RMS duration of 30 fs. The space-charge field on the cathode is estimated as $E_{SC} = 1.2 \cdot Q/(\epsilon_0 \pi R^2)$. For R $<$ 130 µm, the shaded area on the left, less than 16 pC of charge is extracted because of the formation of the virtual cathode due to the strong longitudinal space-charge force E_{SC}.

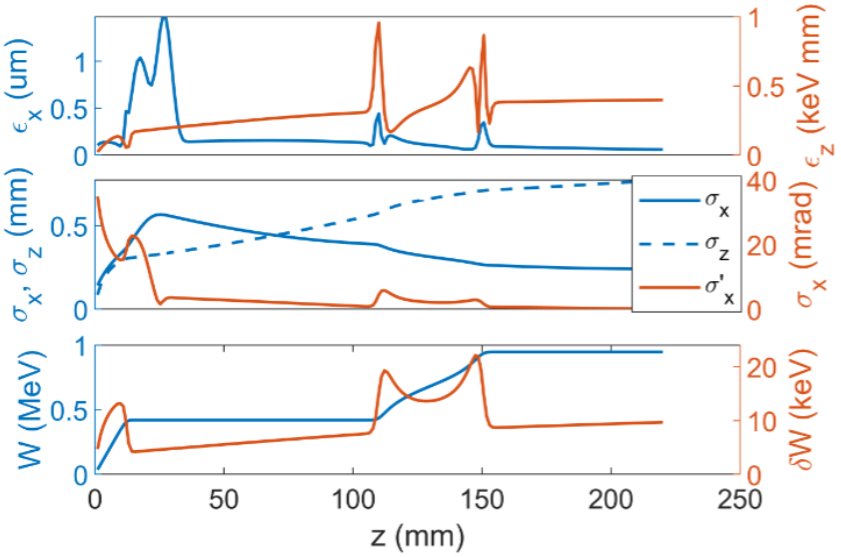

Figure 3.7: Evolution of the bunch parameters in the injector: the transverse and longitudinal emittances, ϵ_x and ϵ_z; the transverse and longitudinal bunch size σ_x and σ_z; divergence σ'_x, the bunch energy W and its spread δW.

3.2.2 Booster

The gun is immediately followed by a normal conducting booster (see Fig. 3.8) at the same frequency of 325 MHz. The booster increases the bunch energy to 1 MeV in order to reduce the space-charge force through the relativistic effect. We found that the emittance is preserved on a 60-nm scale for 16 pC bunches, Fig. 3.7. A small magnetic lens at the gun exit is added to focus the bunch into the booster operated on the crest. Simulations with neodymium magnets have been performed to demonstrate that the required magnetic field can be produced (Fig. 3.9).

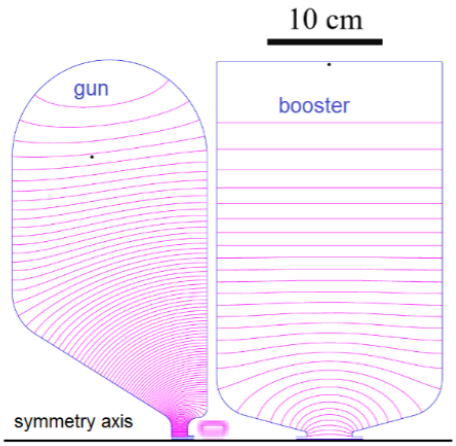

Figure 3.8: Geometry of the injector composed of the gun, a normal conducting booster and a small magnetic lens in between.

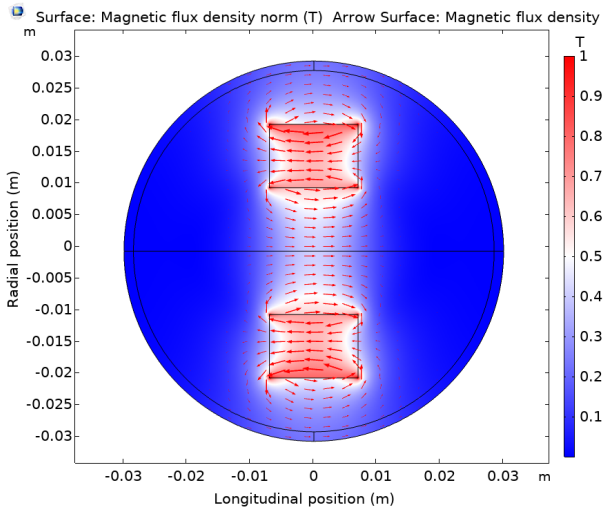

Figure 3.9: Possible solution for a compact magnetic lens based on a ring-shaped neodymium magnet. A thin solenoid can be added for tuning.

3.2.3 Main accelerator: in-cavity ballistic bunching

The low energy of the electron beam upon the injection into the TESLA cavity allows for an unusual regime of bunching in the cavity [7]. The bunch is injected into a deaccelerating phase of the field and because of the velocity mismatch slips further into strong deacceleration, see Fig. 3.10. Simultaneously, the bunch acquires an energy chirp needed for ballistic compression while its energy is dramatically reduced down to around 100 keV. Thanks to this extreme low

bunch energy and the large energy chirp acquired earlier, the longitudinal focusing length is just a few cm. *Specifically, almost all compression occurs within a short distance between 45 and 50 cm from the entrance flange of the TESLA cavity.* After passing the maximum of the de-accelerating field, the bunch slips further into an accelerating phase of the field and in the second cell reaches an ultra-relativistic speed allowing for further synchronous acceleration. Figure 3.11 shows the evolution of the key bunch parameters in the TESLA cavity. Note a drastic change in the bunch duration. Figure 3.12 is a zoom-in into the bunching region. It is interesting that the longitudinal emittance is strongly reduced during the compression. Plots in Fig. 3.13 depict the bunch distribution in different planes of the phase space and give further insight into the bunch compression. There is a noticeable growth of the transverse emittance but the large part of it is correlated and can be removed downstream the accelerator.

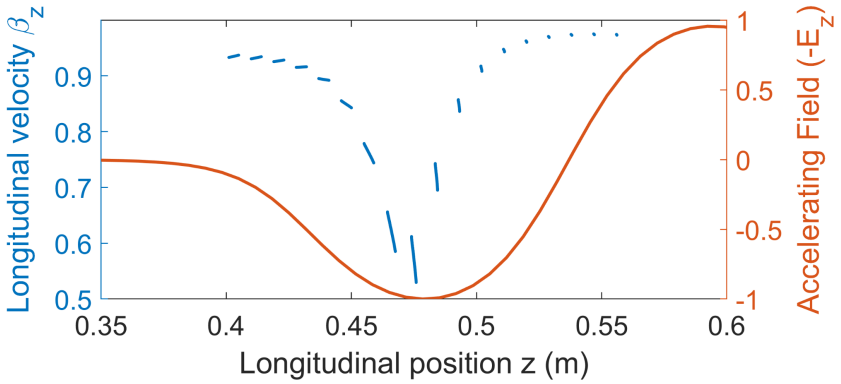

Figure 3.10: Evolution of the longitudinal bunch distribution (blue) in the first cell of the TESLA cavity. The instantaneous distribution of the accelerating field is shown in red.

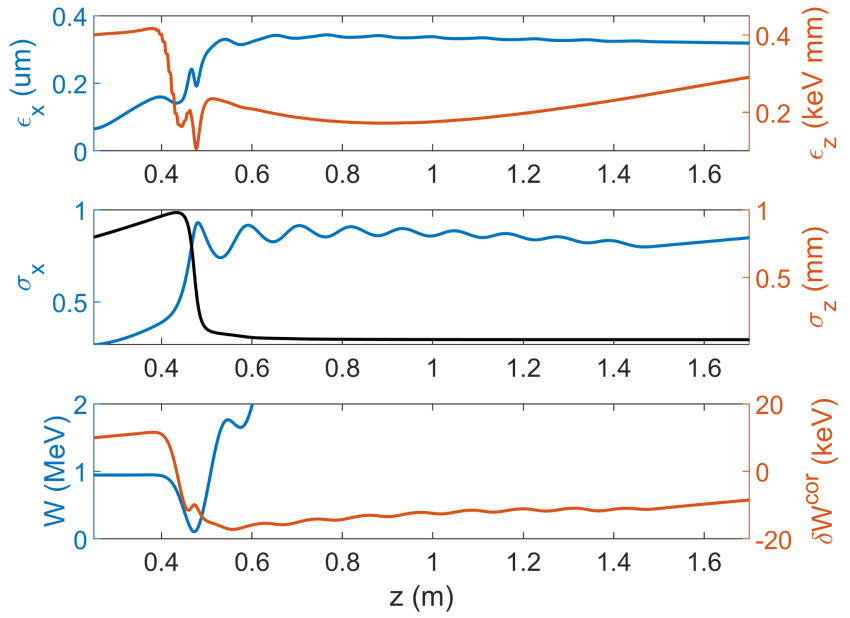

Figure 3.11: Evolution of the bunch parameters in the TESLA cavity: the transverse and longitudinal emittances, ϵ_x and ϵ_z; the transverse and longitudinal bunch size σ_x and σ_z; divergence σ'_x, the bunch energy W and its spread δW.

We have scanned the accelerating field and phase of the TESLA cavity and found that the in-cavity ballistic bunching is robust, see Fig. 3.14. In the figure, the minimum bunch duration as a function of the accelerating field is shown for different values of a focusing magnetic lens

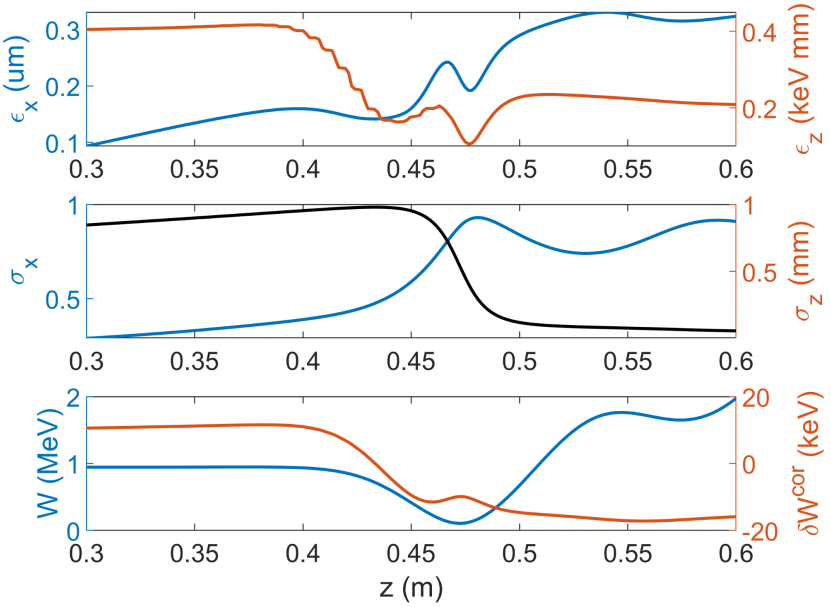

Figure 3.12: Same as Fig. 3.11 but with zoom-in into the region of bunching.

used for injection of the bunch into the TESLA cavity. The strength of the magnetic lens in the injector is an additional control parameter. Figure 3.15 shows a Pareto front for the minimum emittance vs the bunch length. The data are extracted from the scans over the accelerating field.

3.2.4 Energy tuning and focusing

The last unit of the accelerator comprises a 3-cell cavity and a focusing magnetic lens. The cavity allows changing the beam energy by ±6 MeV with the maximum required *accelerating field* of 55 MV/m (gradient ∼27 MV/m), which is well accessible by the present SC technology. The evolution of the bunch parameters around the point of the maximum transverse focusing is shown in Fig. 3.16. A series of the bunch distribution around the focusing point is depicted in Fig. 3.17. The duration of the current density is around 100 fs FWHM. The RMS bunch radius is around 3.5 µm. There is a residual correlated emittance and the bunch focusing is achieved at slightly different longitudinal positions. Further optimization work is needed.

3.3 Electron-beamline upgrade possibilities

A second electron beamline placed in parallel with the original one is envisioned as a future upgrade. It uses magnetic compression to produce highly compressed electron bunches of the order of 10 fs duration. In the following two sections the magnetic compression and the transverse focusing of the electron beam is described and the results of ASTRA simulations applied to these systems are presented.

3.3.1 Magnetic compression

The most common type of magnetic compressor is the chicane, which is illustrated in Fig. 3.18. In the chicane an arrangement of four dipole magnets creates a longer pathlength for the lower-energy electrons, which are more strongly bent by the dipoles, compared to those with higher energy. Thus, an initially (negatively) chirped electron bunch can be compressed.

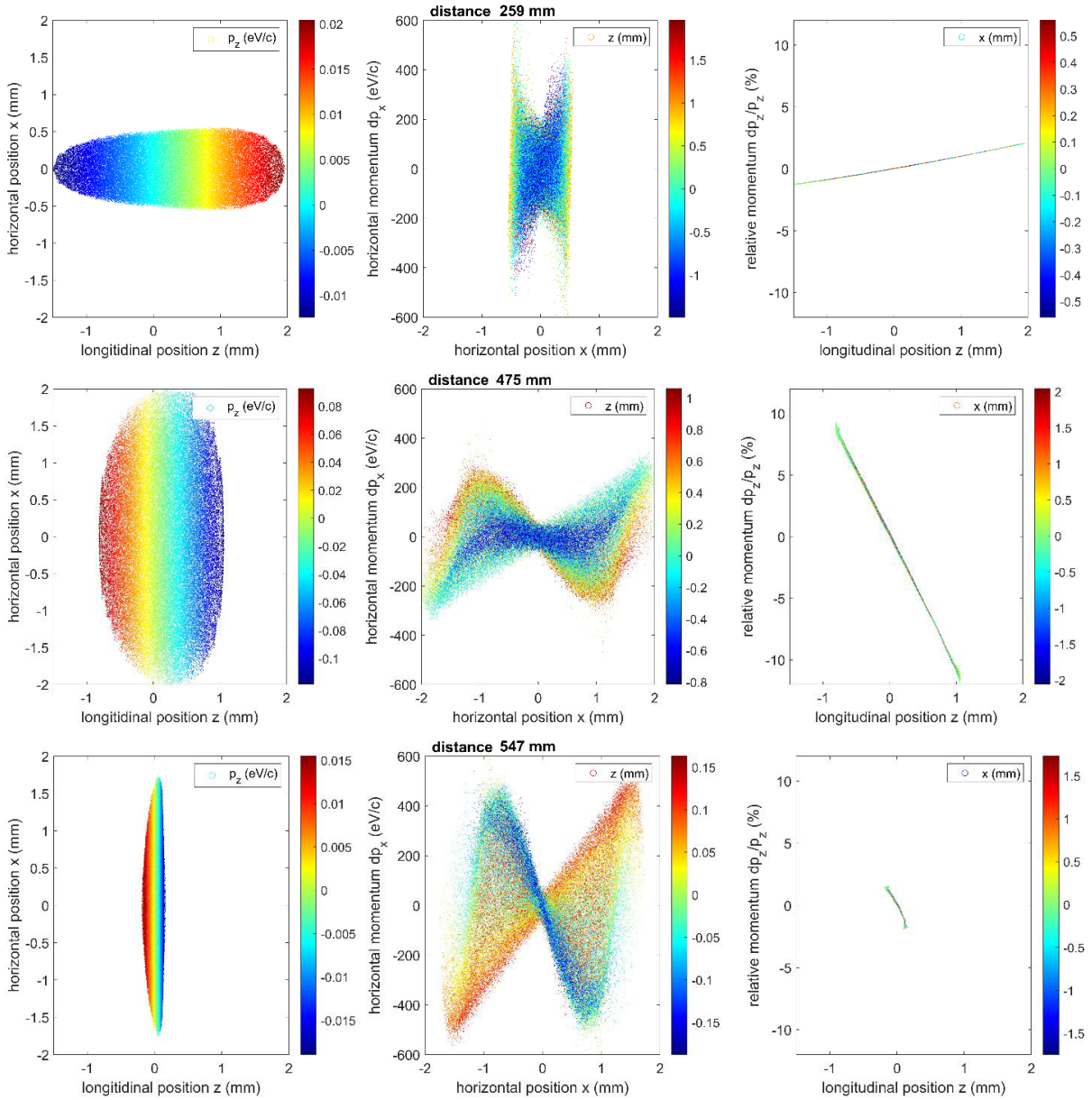

Figure 3.13: Bunch distribution at different positions in the TESLA cavity. The left row shows the bunch distribution in the x-z plane with the color coding used to indicate the longitudinal momentum of the electrons relative to the average longitudinal momentum of the bunch. The middle row shows the phase space x-p_x with the color coding for the longitudinal positions of the electrons relative to the center of the bunch. The right row shows the relative longitudinal momentum of the electrons. The distributions are given at the positions specified in the middle row relative to the entrance flange of the TESLA cavity. We note that in this document we quote the accelerating field not the accelerating gradient, which is approximately half of the field. This implies that the operating gradient of the TESLA cavity is 20.25 MV/m, which is below the operational gradient at the European XFEL.

An efficient alternative way to compress the bunch and simultaneously create an offset with respect to the first beamline is to use a dogleg compressor. It comprises two dipoles with quadrupoles typically placed between them in order to remove the transverse dispersion at the exit of the compressor. This may be an option for the second beamline, however, as a first estimate of the magnetic compression performance we carry out simulations using the chicane-

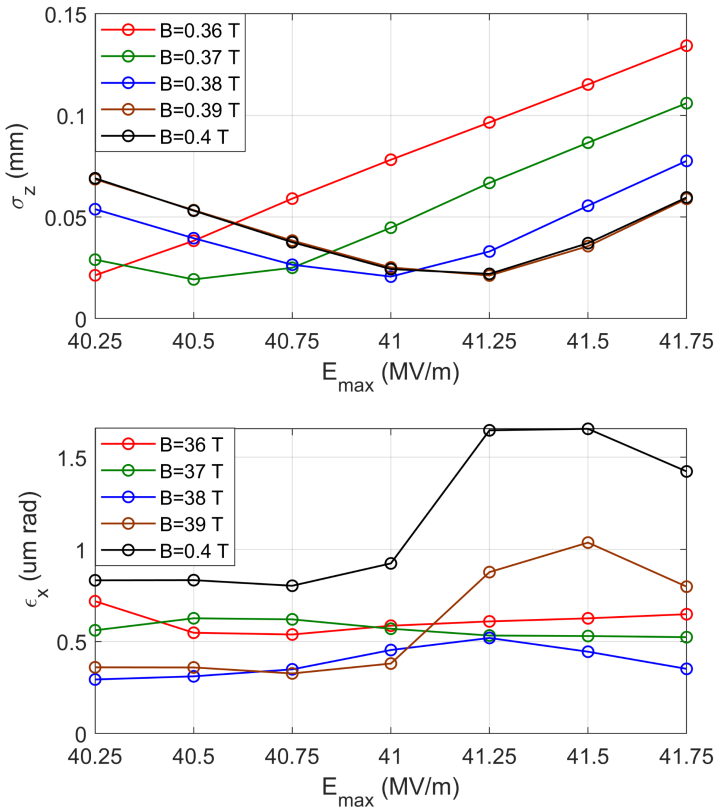

Figure 3.14: Bunch length and transverse emittance at the exit of the TESLA cavity vs the *accelerating field* for several values of the magnetic lens strength in the injector.

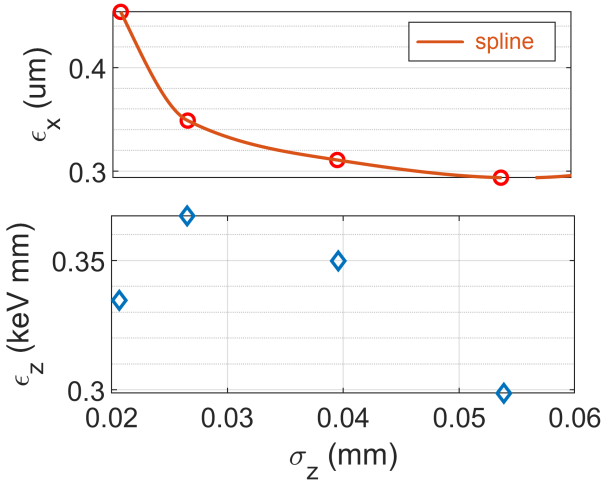

Figure 3.15: Parametric plots of the transverse and longitudinal emittances as a function of the bunch length with the accelerating gradient being the parameter. The data are extracted from Fig. 3.14.

type compressor. In the following, the chicane is considered to be oriented in the horizontal plane, i.e., the electron beam is angularly dispersed in the horizontal direction (x-direction).

The simulations are based on the setup sketched in Fig. 3.19. Two Tesla 9-cell superconducting cavities located before the chicane accelerate the beam to 26.3 MeV. A 9^{th} harmonic cavity following the linac linearizes the longitudinal phase space in order to maximize the bunch

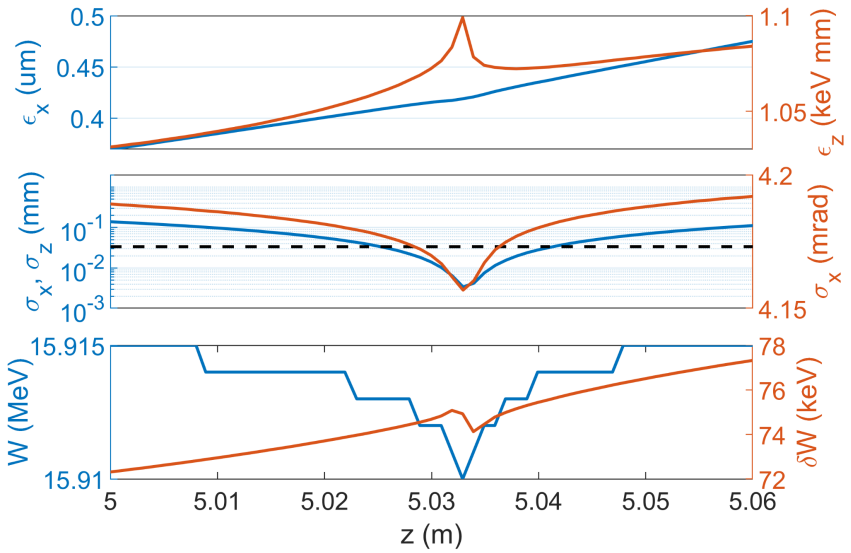

Figure 3.16: Evolution of the bunch parameters in the vicinity of the maximum transverse focusing.

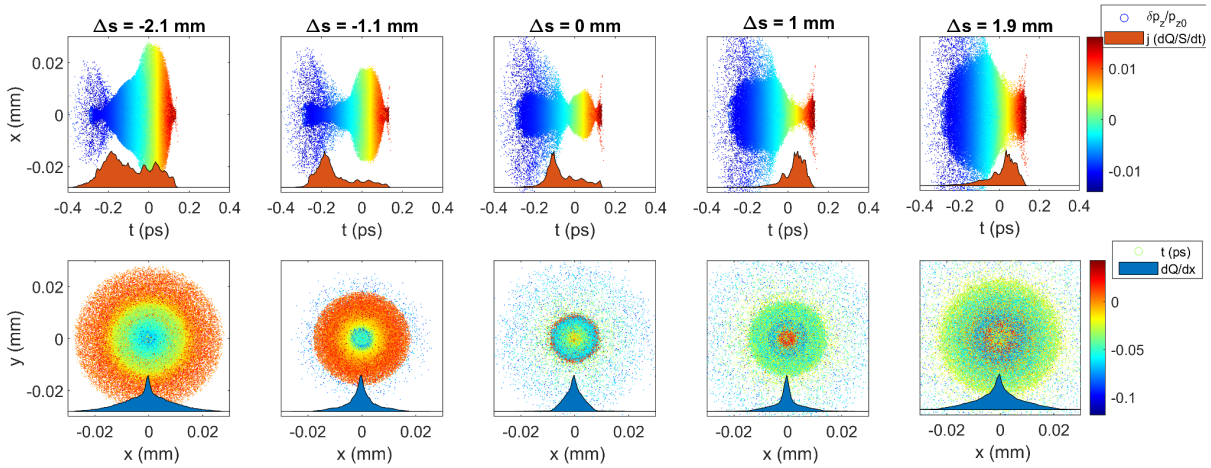

Figure 3.17: Scatter plots of the bunch distribution in the x-t plane (upper row) and in the x-y plane (bottom row). The upper row of the plots also contains the histograms of the current density while the histograms of the bunch distribution projected onto the x-axis are shown in the bottom row.

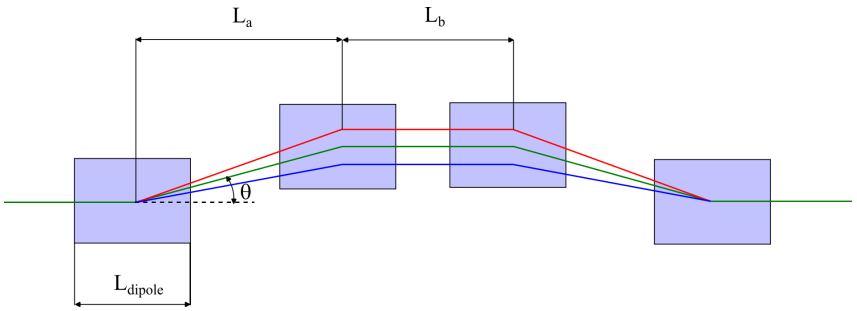

Figure 3.18: Schematic of the chicane compressor. An initially chirped electron bunch is compressed by creating a longer pathlength for the lower-energy electrons (red line) compared with the higher-energy electrons (blue line).

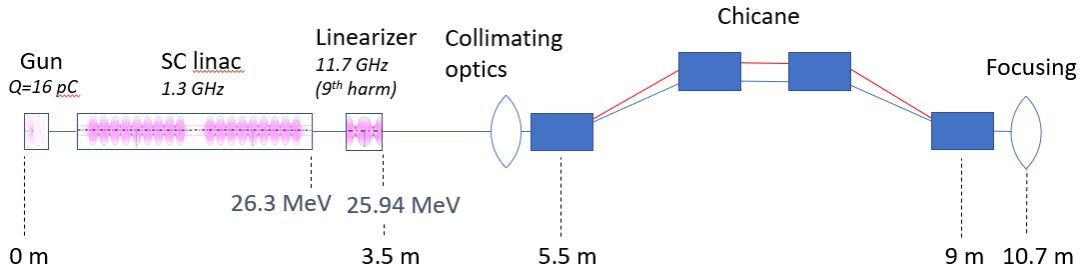

Figure 3.19: Overview of the electron beamline used in simulations of magnetic compression.

compression in the chicane. Figure 3.20 shows the longitudinal phase space (top row) and current distribution (bottom row) before the chicane (left), after the chicane (middle) and at the transverse focus position (right). Table 3.5 summarizes the electron-bunch parameters at the three positions. The chicane parameters are specified in Table 3.6.

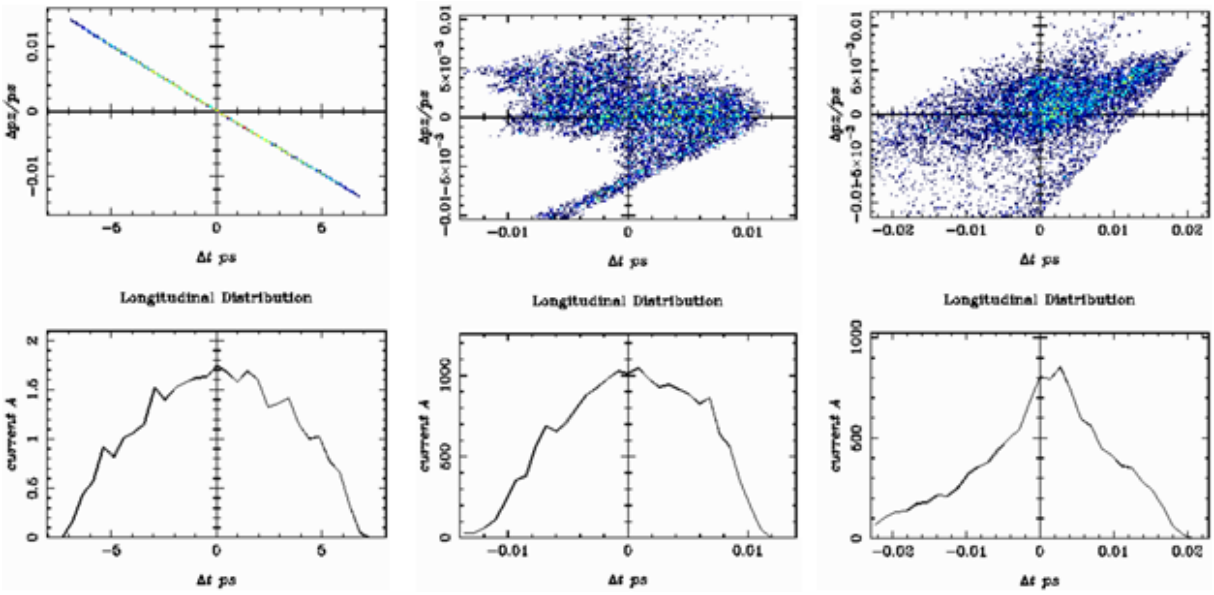

Figure 3.20: Longitudinal phase space (top row) and longitudinal current distribution (bottom row) before the chicane, z=3.5 m, (left panel), after the chicane, z=10.4 m, (middle panel), and at the transverse focus position, z=10.67 m, (right panel).

Table 3.5: Electron-bunch parameters before the chicane, after the chicane, and at the transverse focus position.

Bunch parameter	**Before chicane, after linearizer (z=3.5 m)**	**After chicane (z=10.4 m)**	**At focus position (z=10.67 m)**
Charge (pC)	16	16	16
Energy (MeV)	25.94	25.95	25.94
Rel. energy spread (%)	0.7	0.7	0.7
Emittance (mm mrad)	0.074 (x); 0.075 (y)	0.17 (x); 0.21 (y)	1.05 (x); 0.31 (y)
Duration (fs) RMS/FWHM	3200/6600	5.5/16.5	9.0/15.2

Table 3.6: Chicane parameters as defined in Fig. 3.18.

Dipole magnet length, l_{dipole}	0.7 m
Beam bending angle at dipole magnet, θ	15.28°
L_a	1.2 m
L_b	1.0 m
R_{56}	0.17 m

3.3.2 Focusing

Collimation of the electron beam before the chicane and final transverse focusing was performed using triplet quadrupole systems. The triplet quadrupole focusing system is an efficient method for achieving small and symmetric electron-beam spot sizes. An example of such a setup comprising a defocusing lens between two focusing lenses is illustrated in Fig. 3.21. The distances L_i and focal distances f_i in Fig. 3.21 can be optimized with respect to minimum focused beam size, where L_1 and L_2 are the distances between the first and second lens, and the second and third lens, respectively, while L_3 is the distance from the third lens to the focusing position. For a collimated beam with equal beam size in the x and y-direction the minimum beam size is achieved for L_1=L_2=L_3=f_2=f_3=f_{min} and f_1=2f_{min}, where f_{min} is the minimum achievable focusing length [8]. Here f is related to the quadrupole field gradient, g [T/m], by f=1/[(0.29*g/E)*T], where the E [GeV] is the beam energy and T is the thickness of the quadrupole [9]. Using this design philosophy a focused RMS beam size of 4.8 μm in the x-direction and 2.8 μm in the y-direction was achieved. Figure 3.22 shows the transverse distribution of the electron bunch at the focus position. Table 3.7 lists the parameters of the triple quadrupole system.

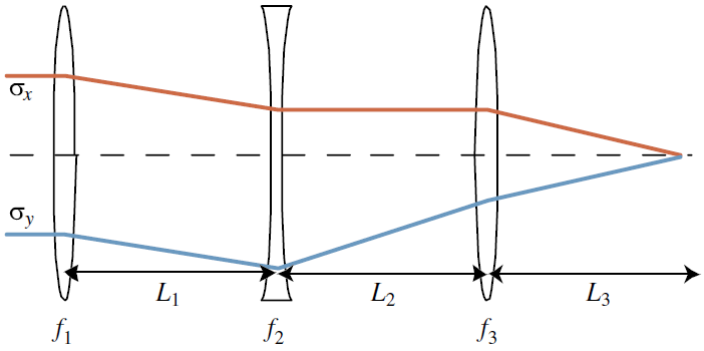

Figure 3.21: Schematic of the triple quadrupole focusing system [8].

Table 3.7: Parameters of the triple quadrupole systems.

Parameter	Collimating triplet quads	Focusing triplet quads
Position (m) 1^{st}; 2^{nd}; 3^{rd} quad	4.5; 4.62; 4.75	10.5; 10.57; 10.64
Quadrupole thickness (m)	0.1	0.05
Field gradient (T/m) 1^{st}; 2^{nd}; 3^{rd}	1.3; 2.6; 1.45	20; 45; 64.5
Focal length (m) 1^{st}; 2^{nd}; 3^{rd}	0.70; 0.35; 0.63	0.091; 0.040; 0.028

3.4 Optical undulator and production of X-rays

In order to produce high X-ray flux by an undulator, the undulator strength parameter, K, must be sufficient. For the optical undulator, the K value is proportional to the B-field produced

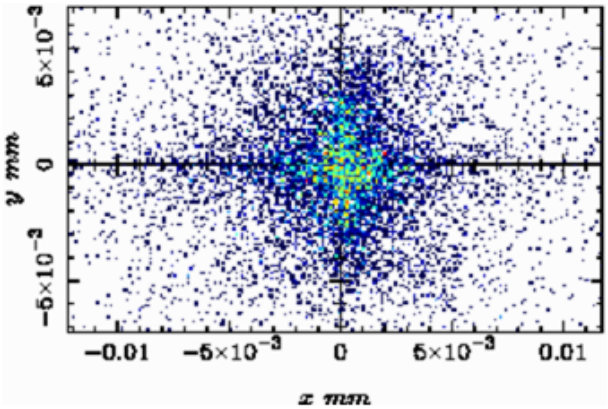

Figure 3.22: Transverse electron-bunch distribution at the focus position (z=10.67 m).

by an optical laser. A typical approach to achieve a strong B-field implies using pulsed radiation with high pulse energy and short pulse duration as well as tight beam focusing. However, excessive focusing leads to quick beam expansion and light intensity decrease away from the focal plane, which reduces the generated X-ray flux. Therefore, the laser beam focal spot has to be balanced against the depth of focus.

The above criteria are the key points to specify requirements to the driving laser for the optical undulator of the inverse Compton source. Operating at a repetition rate of 100 kHz, the laser should generate Fourier-limited pulses at a wavelength of 1030 nm with pulse energies of at least 50 mJ at a pulse duration of $\sim$1 ps (FWHM). Promising candidates for high-power lasers are based on so-called thin-disk (TD) technology [7]. The laser beam then should be focused onto a spot of the order of 10 µm in diameter, which offers a suitable depth of focus of similar length as the pulse duration.

The parameters of the inverse Compton source are calculated using the model of spontaneous undulator radiation for the effective equivalent magnetic undulator [10, 11]. The results are presented in Table 3.8. The electron bunch is assumed to be moderately compressed to provide the minimum broadening of the inverse Compton X-ray spectrum through the energy spread effect. The ponderomotive broadening is assumed to be compensated for by chirping the laser pulse. The natural broadening of on-axis radiation due to 3D effects [12] amounts to 0.42%. The analytically estimated number of X-ray photons per pulse at 1 nm into 0.1 eV bandwidth is 780. This number can be tripled by increasing the laser pulse energy to 500 mJ while reducing the repetition rate to 10 kHz.

For cross-checking, numerical simulations with the simulation code Simplex [13] were performed and the results are presented in Fig. 3.23. The photon flux per shot into *0.1 eV bandwidth* is around 700 photons which is consistent with the analytical estimate. Note that the transverse profile of the average power density has a speckle pattern due to the stochastic nature of spontaneous radiation. The power density distribution changes from shot to shot.

3.5 X-ray beamline

The X-ray photon beamline is designed to enable a broad class of experiments including spectroscopy, scattering and pump-probe studies to address the questions formulated in the science cases described above in chapter 2. For this purpose, the beamline comprises two sections named broadband and mono (monochromatic), which are schematically shown in Fig. 3.24. The broadband beamline delivers the full X-ray spectrum of the source and allows higher flux, while the mono beamline provides high spectral resolution by selecting a narrow X-

Table 3.8: Simulated parameters of the inverse Compton source at 0.25 nm (4.8 keV) corresponding to the case of the 16 MeV electron bunch discussed in detail earlier. The electron bunch parameters are depicted in blue, the laser parameters in red, and the X-ray yield in black.

	Parameter	Symbol	Value	Units
Electron beam parameters	Electron bunch charge	Q_b	16	pC
	Number of electrons	N_b	10^8	
	Bunch energy	U_b	16	MeV
	Relative energy spread	δ_γ	0.5%	
	FWHM bunch duration	τ_b	< 200	fs
	Bunch emittance	ϵ_n	0.4	mm· mrad
	RMS bunch size	σ_b	3.5	µm
	Geometrical beta-function	β_g	$\sim$2	mm
Laser beam parameters	Laser wavelength	λ_L	1.0	µm
	FWHM laser pulse duration	τ_L	2.35	ps
	RMS laser beam size	σ_L	4.9	µm
	Rayleigh length	z_R	0.3	mm
	Laser pulse energy	ε_L	50	mJ
	Undulator parameter	κ	0.14	
	Laser rep. rate	f_L	100	kHz
X-ray yield	Radiation wavelength	λ_r	0.25	nm
	Photon energy	E_{ph}	4.8	keV
	FWHM X-ray pulse duration	τ_X	< 200	fs
	RMS X-ray beam size	σ_X	3.7	µm
	Opening angle of radiation cone	θ	1.75	mrad
	BW of acceptance cone, RMS	BW_{cone}	1%	
	X-ray photons/shot	N_{ph}	$2.2{\cdot}10^4$	
	X-ray photons/second/0.1%BW	$F_{0.1\%}$	$7.4{\cdot}10^8$	
	Average spectral density within θ	D	$6.7{\cdot}10^6$	ph/s/eV

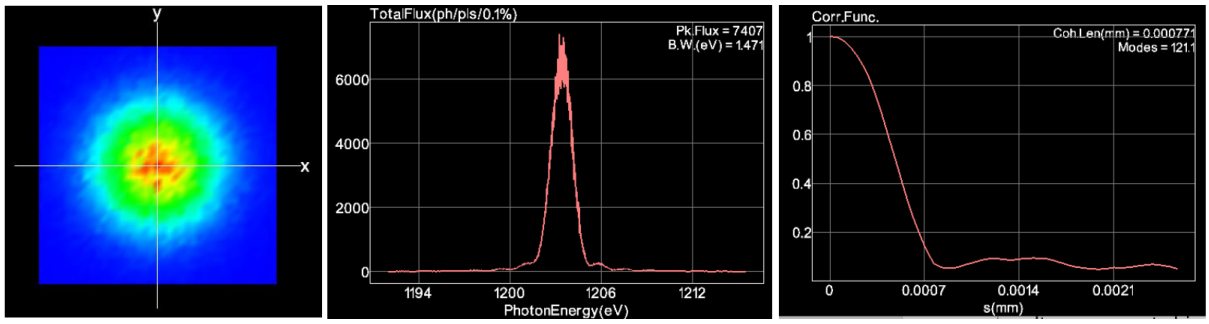

Figure 3.23: Simulation results for the inverse Compton source using the Tanaka code Simplex [13]. From left to right: the power density averaged over the pulse as a function of transverse coordinates, the photon flux per shot vs photon energy, and the temporal correlation functions of the 1st order as a function of distance.

ray bandwidth using a monochromator. One envisioned experimental station for each beamline is indicated in Fig. 3.24. The main X-ray parameters of the source, and the broadband and mono beamlines are summarized below their appearance in Fig. 3.24 and in more detail in Table 3.9.

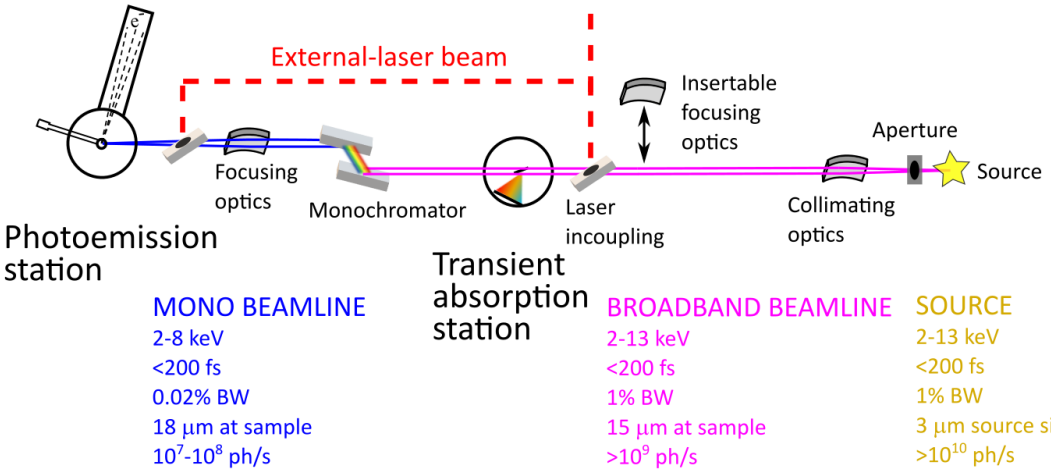

Figure 3.24: Schematic layout of X-ray beamlines and calculated X-ray beam parameters for the Ångström Laser baseline version. The influence of X-ray optical elements was taken into account using ray-tracing simulations [14]. With two experimental end stations for ambient pressure photoemission (using monochromatized X-ray radiation) and for transient X-ray absorption (using broadband X-ray radiation) and on-demand replacement of the ambient pressure photoemission end station with a momentum microscope and the transient absorption with an X-ray scattering setup, all science cases described in chapter 2 can be addressed.

Table 3.9: Photon-beamline X-ray parameters using the optics specified in Table 3.10. The source brilliance is given for 100 kHz repetition rate.

Parameter	**Broadband**		**Mono**	
Photon energy (keV)	2	13	2	8
Transmission %	37	19	0.19	0.92
Flux (ph/s)	$4x10^9$	$2x10^9$	$2x10^7$	$9x10^7$
Focused beam size (µm) RMS	18x18	13x13	20x20	17x17
Pulse length (fs) FWHM	<200			
Resolution (eV)	20	130	0.31	2.1
Polarization	Linear in baseline design (upgradable)			
Source brilliance at 8 keV (ph s^{-1} (0.1% bw) mm^{-1} $mrad^{-1}$)	$4x10^{13}$			

3.5.1 Optical layout overview

The optical components of the beamlines are shown in Fig. 3.24 and Table 3.10 provides further details of all the beamline optics. Raytracing simulations of the optics influence on the X-ray beam were performed using RAY [14]. The first photon-beamline component is a variable aperture placed 0.1 m after the source point. It allows modifying the bandwidth and flux by selecting the transmitted divergence angle of the X-ray beam. The X-ray beam is subsequently collimated using capillary optics placed 0.25 m after the inverse Compton source. The collimation permits propagation of the X-ray beam at a constant size of ∼2 mm FWHM to the optical components located further downstream behind the radiation-safety wall. The first suggested experimental station is the transient-absorption station, which requires the full X-ray bandwidth to fully cover absorption edges of relevant elements in the corresponding X-ray energy range and it is thus placed before the monochromator. Focusing optics reduces the beam size to

$\sim$15 µm RMS at the sample. We note that the transient-absorption end station could be exchanged with an X-ray diffraction and scattering end station to make accessible new science cases in the future.

Table 3.10: Specifications of optical components of the photon beamlines. The incidence angles are specified as grazing incidence. A surface roughness of 3 Å and a slope error of 0.5 µrad have been assumed in all simulations using these optics.

Parameter	**Aperture**	**Collimating optics**	**Focusing optics**	**Laser incoupling mirrors**	**DCM (Si[111])**
Distance from source (m)	0.1	0.25	broadband 8.2; mono 13.3	8.6 13.7	11.3
Focusing distance (m)		inf.	broadband 1.0; mono 1.2		
Shape		parabolic monocapillary	paraboloid mirror	plane mirror	
Size (mm)	variable	entr. diam.=0.8 length=300	width=20 length=600	diam.=25 hole diam.= 3	
Inc. angle (°)		0.07 at center	0.2	45	14-81

In order to transport the beam to the downstream photoemission stations (ambient-pressure photoemission or momentum microscopy depending on the user demand) the focusing mirror and optical components in the transient-absorption station can be retracted. A double-crystal monochromator (DCM) is placed downstream of the transient-absorption station. It provides a narrow spectral bandwidth of $\sim$0.02% for the photoemission experiments. Focusing of the beam to a $\sim$18 µm RMS spot at the sample position is accomplished by another focusing optic placed after the DCM, while the upstream focusing optic is retracted. Both the transient absorption and the photoemission station have incoupling mirrors for the external-laser pump beam, which are located between the respective focusing optic and the experimental chamber. The laser-in-coupling mirror has a hole in the center that allows the X-ray beam to pass and enables collinear incidence of the pump and probe beam on the sample for optimal temporal resolution in the pump-probe experiments.

3.5.2 Focusing optics

A collimating optic is placed close to the inverse Compton source in order to avoid excessive increase of beam size. A monocapillary optic will be used, which consists of a glass capillary that collimates the X-rays by total external reflection at rotational parabolic surfaces as illustrated in Fig. 3.25. This design allows compactness and a high transmission at a broad photon-energy range. A monocapillary of 300 mm length and 0.8 mm inner entrance diameter will be employed, which provides $\sim$20-40% transmission over the full 2-13 keV interval.

The focusing optics just upstream of the end stations will provide a small spot at the sample. A paraboloid mirror (Fig. 3.26 top) is considered the optimal choice in this case. The main reason is that, in contrast to the collimating mirrors described above, the focusing mirrors can be made relatively long (600 mm) since there is more available space. In this case the paraboloid covers most of the beam size and then produces higher transmission compared with the monocapillary optics. Another option is using Kirkpatrick-Baez (KB) mirrors, i.e., two plane-parabolical mirrors reflecting in the horizontal and vertical plane, respectively. They can either be placed after each other or more compactly in Montel configuration (Montel optics) as shown in the bottom panel of Fig. 3.26. The first choice, in-line KB configuration, is more

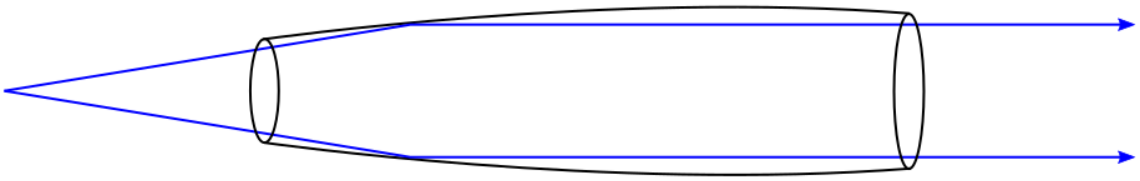

Figure 3.25: Illustration of monocapillary optics for collimating the X-ray beam (one set of possible X-rays is shown).

flexible since it allows adjusting each mirror separately. It is a standard focusing technique at synchrotrons and free-electron lasers. The disadvantage is the required length, although sufficient space exists to extend the beamline to include in-line KB mirrors.

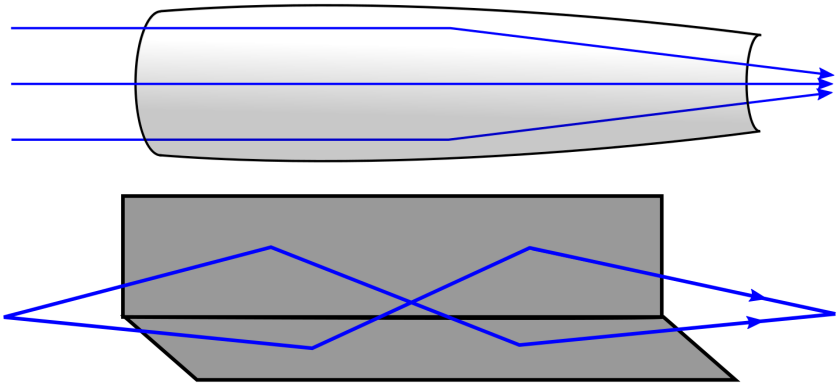

Figure 3.26: Illustration of two possible types of focusing optics, a paraboloid mirror (top) and Montel optics (bottom).

In order to obtain high reflection from the focusing optics a small grazing incidence angle of $\sim$0.2° is used. The coatings have to be adapted to the different photon-energy regions. B_4C coating provides almost 100% reflection at 2-8 keV but drops rapidly at higher photon energies. Therefore, rhodium coated mirrors will be employed at higher photon energies, which ensures >90% reflection at 8-13 keV. This extra set of rhodium coated focusing optics will be provided for the broadband beamline in the baseline design.

3.5.3 Monochromator

The mono beamline includes a monochromator that creates a narrow X-ray bandwidth for spectrally resolved measurements. The target photon-energy range of the monochromator is 2-8 keV. For such high-energy X-rays a double-crystal monochromator (DCM) is typically used. It comprises two crystals oriented such that a small photon-energy region is selected upon double Bragg reflections. Using Si(111) crystals the full 2-8 keV interval of the mono beamline can be scanned by orienting the crystals to X-ray grazing-incidence angles between 14 and 81 degrees. Fixed beam exit-height can be provided by translation of the crystals along the beam direction during the photon-energy scans. The simulated photon-beam parameters of the mono beamline are shown in Fig. 3.27.

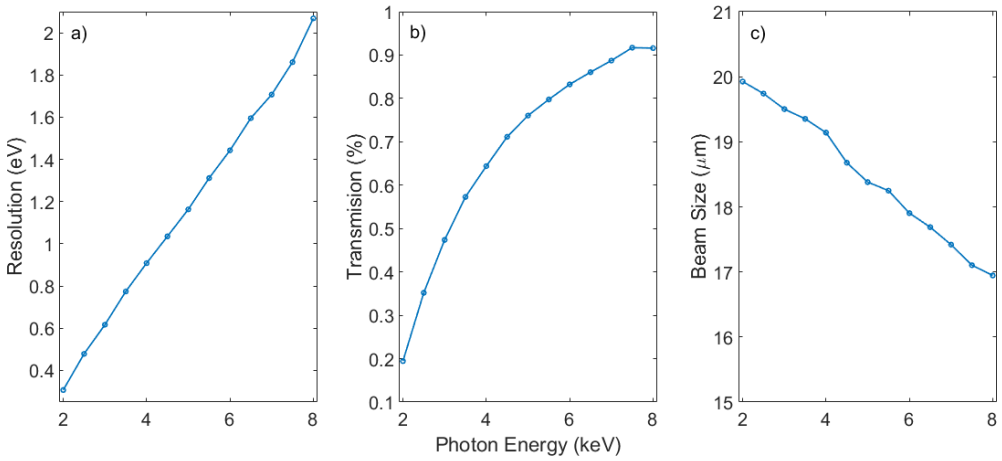

Figure 3.27: Mono beamline output parameters using a Si(111) double-crystal monochromator obtained by ray-tracing simulations [14] using the optics specified in Table 3.10. (a) Resolution, (b) transmission at the sample position with respect to the X-ray source, (c) focused RMS beam size at the sample position.

3.5.4 Laser in-coupling

The laser in-coupling mirror will be located between the X-ray focusing optics and the end station. It will have a hole in the center that transmits the X-ray beam while the remaining surface reflects the optical beam. The hole has to be sufficiently large to avoid clipping of the X-ray beam but still provide a high incoupling efficiency of the laser beam. Therefore, a hole diameter corresponding to an X-ray beam size of 6σ ($\sim$3 mm) at the in-coupling-mirror position can be used. This offers a laser incoupling efficiency of $\sim$94% assuming a laser beam width of 10 mm FWHM.

3.5.5 Optical lasers

The pump beam for the end stations is generated by either an industrial-grade solid-state femtosecond laser, CARBIDE-CB3-80W, or optical parametric amplifiers (OPAs). Both the laser and OPAs are produced by Light Conversion UAB. These lasers for pump-probe experiments already exist and an upgrade to pump lasers with shorter pulse durations is foreseen.

The CARBIDE laser is seeded by an external optical oscillator, FLINT, which is locked to a repetition rate (RR) clock at 1.3 GHz to generate seeding pulses at the 65 MHz RR. An embedded pulse picker and power amplifier allow CARBIDE to operate at the 0.1-100 kHz RR and produce up to 80 W of average power into a diffraction-limited beam at the 1030 nm (1.2 eV) center wavelength with the FWHM pulse duration of 200 fs.

Approximately half the CARBIDE laser power (40 W) is outcoupled to optically pump ORPHEUS-ONE-HP OPA. The OPA generates an infrared beam with an output power of up to 7 W, which is spectrally tunable in the 1.3-18 µm wavelength range. An additional OPA with a harmonics generator will enable it to reach shorter wavelengths (down to 210 nm) and expand the tuning range to the visible and UV regions. An external pulse picker together with compressor/stretcher provide wide options to control sequences and duration of the OPA pulses. Accompanied with an ultra-broad tuning range, 0.07-5.9 eV, this enables it to fulfill the user requirements to the pump beam for most of the experiments. The far IR region and THz light frequency range will be reached with a light source based on nonlinear optical rectification in crystals.

Higher light fluxes in the visible and UV, which are necessary for some experiments, are provided by the CARBIDE laser fundamental harmonics and its frequency sidebands. Specifically, with the 40 W mean power (the second portion), the 2^{nd}, 3^{rd}, 4^{th}, and 9^{th} frequency harmonics, generated in the beta-barium borate (BBO) crystals and noble gases, enable several discrete lines in the range of 2.4-11 eV with peak pulse power of up to 1 GW. Part (1 W) of the 4^{th} harmonics beam is then directed into the photoinjector to produce an electron bunch.

A state-of-the-art high-average power fs system, based on the Yb:YAG crystal TD technology, is used to optically pump the optical undulator. It is a system developed by TRUMPF Maskin AB, which is currently being tested. It comprises TruMicro 2000 drive laser which is synchronized to the FLINT laser oscillator, a TD regenerative amplifier Dira 1500-100, that delivers 1.5 kW at the 100 kHz chirped pulse RR, followed by three multipass amplification cells, each adding 1.5-2.0 kW of power. After the pulse compression down to 1 ps, the TD TRUMPF system should provide 4-5 kW of mean power with 40-50mJ pulse energy.

3.6 Diagnostics

"Any accelerator is only as good as its diagnostics" - as the adage in the accelerator community goes. The commissioning phase will go hand in hand with the characterization of electron bunches and X-ray pulses. The inverse Compton process is determined by the 6D phase space distribution of electron bunches and hence a full phase-space characterization is needed.

3.6.1 Electron-beam diagnostics

Electron-beam diagnostics will be placed at strategic positions along the linac to monitor the beam properties and to provide input for feedback systems. In order to track the electron beam trajectory along the linac several beam position monitors (BPM) are foreseen. BPMs typically measure the signals from a passing beam using four antennas. The stripline-type of BPM is longer ($\sim$150 mm) than the button type and yields a stronger signal. Commercially available BPM electronics connected to the stripline BPM will provide a resolution in the µm range [15].

The electron beam profile is commonly measured with insertable YAG screens. The fluorescent radiation produced by the YAG screens upon electron impact is imaged onto a CCD screen.

The beam current and bunch charge can be monitored nondestructively using current transformers that can provide $\sim$1% resolution [16]. Faraday cups can also be used destructively for absolute charge measurements offering high resolution for small charges.

The beam energy and energy spread can be obtained from the horizontal electron distribution at a YAG or stripline BPM placed after a dipole, which creates a non-zero dispersive function. Thus, BPMs placed after the dipole positioned downstream of the interaction point can function as energy diagnostics.

To obtain slice-by-slice information about a bunch, the bunch is streaked by first imprinting an energy chirp along the bunch and then projecting the bunch on a suitable screen. In a tomographic method [17], the transverse phase space of bunch slices is obtained with several projections of the particle distribution while the beam rotates in the corresponding phase space. Bunch duration and energy distribution (using an energy dispersing magnet) are also measured. There is a plan for installing an X-band transverse deflecting cavity (TDC) after the laser undulator.

A TDC will be used as bunch length and arrival time diagnostic [18, 19]. The TDC will be installed downstream of the interaction point between the laser and electron beams and can thus be operated parasitically. It comprises RF-cavities that deflect the electron bunch with an arrival-time dependent amplitude using a quickly changing transverse RF-field. This leads to a rotation of the electron bunch, which enables mapping of the longitudinal bunch coordinate onto the vertical axis by detecting the electrons on a downstream screen. The expected temporal resolution is below 100 fs [19]. In addition, the TDC can be used for measuring the slice emittance [19].

3.6.2 Electron-beam and laser-beam overlap diagnostics

The electron beams of linac-based inverse Compton sources (ICS) can be produced with a low emittance compared with ring-based ICS. This permits short and transversely small electron bunches. Consequently, the linac-based ICS requires a highly accurate overlap between the electron bunches and optical laser pulses with spatial and temporal precision on the scale of 10 µm and 100 fs, respectively. One existing method to measure the overlap uses a retractable aluminum bevel-edge placed at the interaction point (see Fig. 3.28) [20]. The bevel-edge is positioned such that the electron beam and laser beam, entering from opposite directions, hit close to the edge. The electron beam generates optical transition radiation (OTR) and the laser beam is reflected. By imaging the OTR and the laser beam together on a CCD camera the spatial overlap can be optimized with sufficient precision. Using a semi-transparent mirror both beams can also be directed to a streak camera, which measures the temporal overlap with a sub-nanosecond precision. Although this precision is insufficient by itself, it provides the course timing (within the RF period) for the transverse deflecting cavity, which in turn permits $<$100 fs timing accuracy.

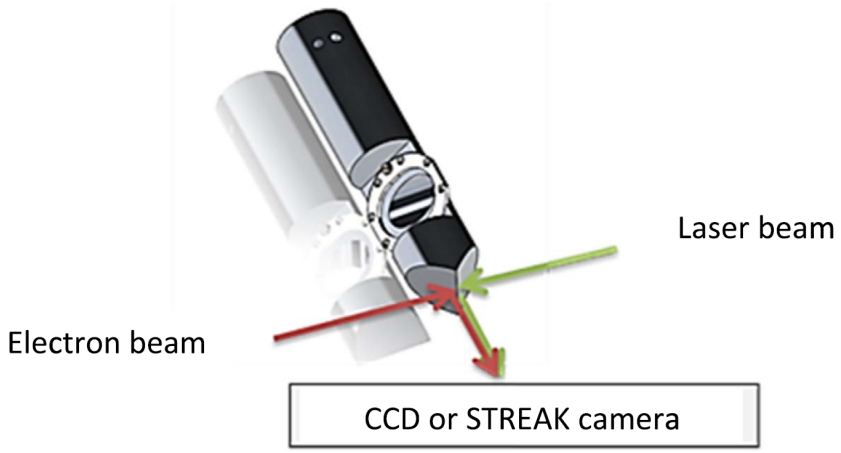

Figure 3.28: Illustration of a potential spatial and temporal diagnostic for electron-beam and laser-beam overlap at the interaction point [20]. A retractable bevel-edge with aluminum surfaces is inserted at the interaction point between the laser and electron beam. The spatial and course temporal overlap is obtained by detecting the co-propagating reflected laser beam and the OTR beam generated at the aluminum surfaces, on a CCD and a streak camera.

3.6.3 X-ray-beam diagnostics

X-ray beam diagnostics are necessary for optimization of the photon beam during commissioning and regular operation. For example, monitors of flux, position and beam profile are required to tune the beamline optics and guide the X-rays to the end stations. Moreover, characterization of the X-ray source parameters such as spectrum, flux, source position and

size are crucial for efficient X-ray generation. The monitoring of the source parameters is particularly important for the inverse Compton source, which sensitively depends on the overlap between electron bunches and optical laser pulses.

The X-ray beam diagnostics of the Ångström laser are schematically shown in Fig. 3.29 and are indicated with green text. The X-ray source size and position will be monitored using a knife edge combined with a CCD camera placed further downstream. This setup exploits the so-called penumbral blurring produced when the rays of an extended light source pass through a knife edge that is imaged at some distance. The source size can be inferred from the degree of blurring of the knife-edge image, while the source position is determined from the position of the edge in the image [21]. In addition, the flux can be monitored by the same CCD camera. This system will be useful for optimizing the electron-laser interaction of the source by tuning their temporal and spatial overlap. The CCD camera by itself, without the knife edge, will also be useful for monitoring the X-ray beam position and size at the location of the camera.

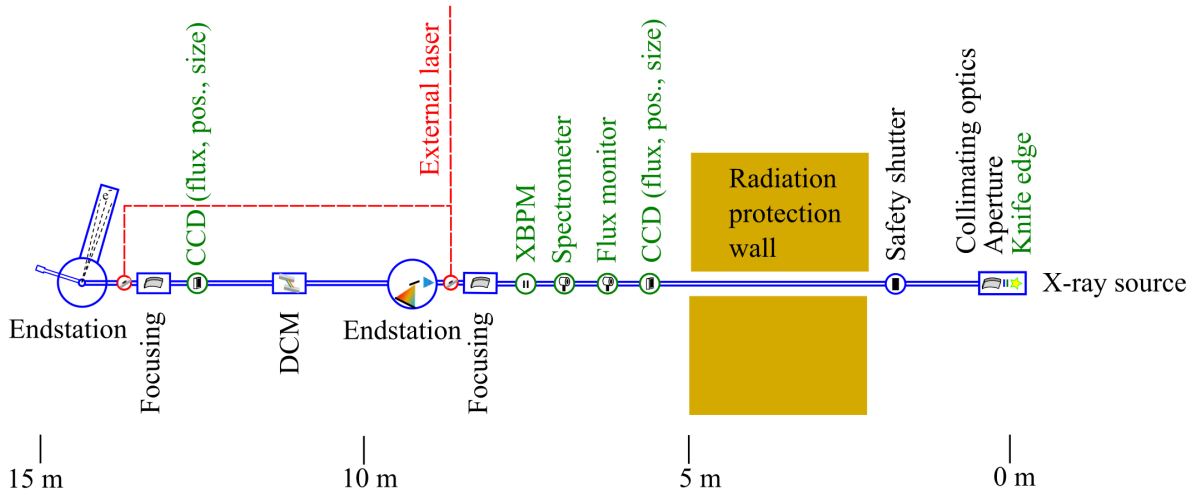

Figure 3.29: Overview of the X-ray beam diagnostics (green text).

CCD cameras for flux, size and position measurements of the X-ray beam will be placed before each end station. Additional 2D detectors can be integrated with the experimental chambers in order to determine the beam parameters at the sample position. The CCD cameras of the beamlines will permit to monitor the flux parasitically using custom designed cameras that intercept the X-rays only slightly at the bottom part of the beam [21]. However, they can also be moved vertically in order to detect the full beam, e.g., for beam position and size measurements. The CCD cameras will measure the relative flux but will be calibrated using Si-PIN diodes [22], which provide the absolute flux. The CCD cameras [23] will be complemented with blade-type X-ray beam position monitors (XBPM) [24]. They permit parasitic operation by measuring the current variations on electrodes interacting with the edges of the X-ray beam. The current is proportional to the area of interaction.

The photon-energy diagnostics will be performed using a Si-drift detector [25], which provides a spectral resolution down to 1%. Measurements of the X-ray pulse arrival time and pulse duration can be obtained to a sufficient precision using the electron bunch diagnostics, which has $<$100 fs accuracy [19] (see also the synchronization and timing section 3.8). Table 3.11 summarizes the main X-ray beam diagnostics envisioned for the Ångström laser and their accuracies.

A beam safety shutter made of tungsten is located before the radiation protection wall (see Fig. 3.29). It prevents the beam from entering the downstream experimental area.

Table 3.11: Summary of X-ray beam diagnostics. Note that the DCM combined with the CCD flux monitor can also be used for measuring the photon energy with an accuracy reaching 0.02%.

Diagnostic	Type	Accuracy
Flux monitor (destructive)	Si-PIN diode [22]	abs. 20%
Flux monitor (parasitic)	CCD [23]	rel. $<$1%
Size monitor (destructive)	CCD [23]	10 µm
Beam position monitor (destructive & parasitic)	CCD [23] (destr.) Blade-type XBPM [24] (par.)	10 µm
Spectrometer (destructive)	Si-drift detector [25]	$\sim$1%
Pulse arrival time and length (parasitic)	From e-bunch [19]	$<$100 fs

3.7 End stations

Table 2.1 maps the scientific drivers onto a set of end stations that can address these science challenges. In this section we describe the envisioned dedicated experiments enabling time-resolved photoemission, absorption and resonant scattering experiments. The various required sample environments will be developed together with the prospective user groups and it will be possible for them to install additional experiments and sample preparation facilities. The envisioned laser pump capabilities are described in section 3.5.5.

3.7.1 X-ray photoemission spectroscopy

We envision element-specific core-level photoemission spectroscopy in the X-ray spectral range to be one of the key experimental methods at the Ångström Laser. Currently, spectrometers for photoemission studies are mainly based on hemispherical electrostatic electron kinetic energy analysis where the relatively low photon count per pulse avoids electronic space charge, often limiting detection at XFELs. It is interesting to note that a spin-off company from Uppsala University (ScientaOmicron) has developed into a market leader for such spectrometers. Here, we will use a radically different approach based on energy analysis via measuring the time of flight of photoemitted electrons. This method efficiently detects photoelectrons and enables operation at the lowest possible X-ray flux, thus, reducing beam damage to sensitive samples. We plan to use two types of time-of-flight spectrometers, one optimized for spatial resolution (momentum microscope) and another (ARTOF) adapted to high-pressure operation.

The momentum microscope was pioneered by Gerd Schönhense (Mainz University) and several instruments developed and built by his team are in operation at synchrotron sources (BESSY II, PETRA III) and free electron lasers (FLASH and in the near future EU-XFEL). It consists of electron optics that can image the full angular distribution of X-ray photoelectrons combined with time-of-flight analysis (3D recording scheme) [26, 27]. This enables an efficient detection of nearly all photoelectrons, in contrast to hemispherical energy analysis where only a section of the k-distribution along one line is detected simultaneously (2D scheme). The instrument can also be operated in a spatially imaging mode where photoelectrons emitted from regions of the sample only several 10 nm apart can be detected and allow to image solid-state devices in-operando. A schematic illustration of the end station [28] is shown in Fig. 3.30. It will be built and commissioned by KTH (Oscar Tjernberg).

The ARTOF spectrometer was developed by ScientaOmicron/Uppsala for operation at VUV pulsed laser sources. We will adopt an existing ARTOF spectrometer to high kinetic energy operation and implement differential pumping stages to enable ambient pressure photoe-

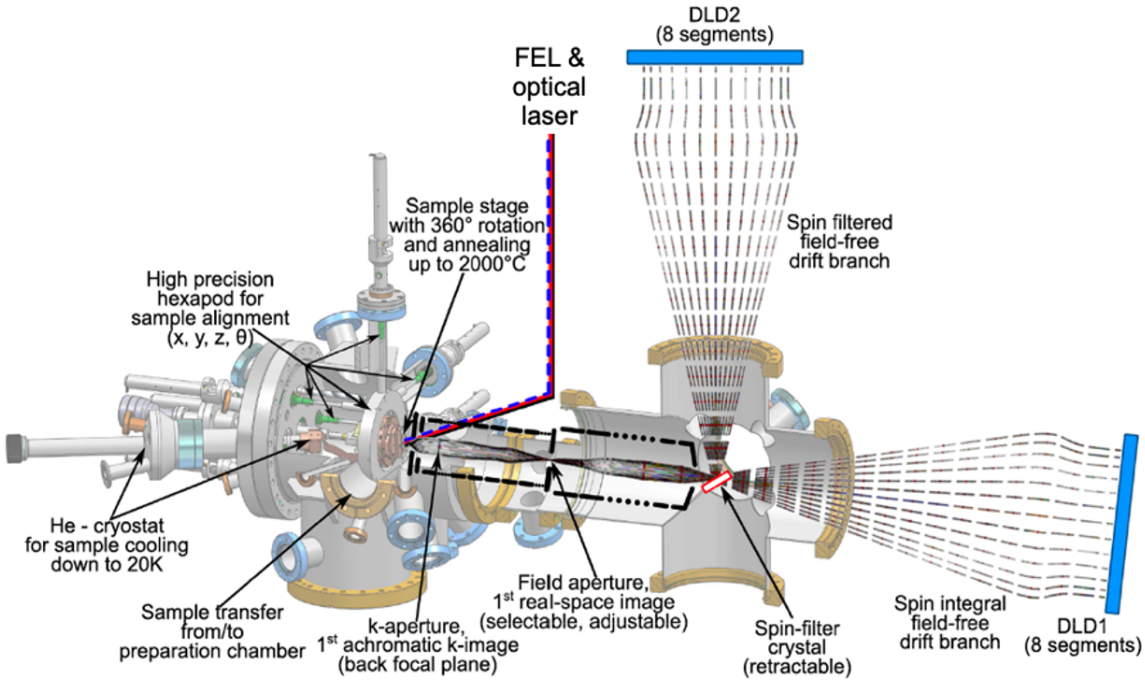

Figure 3.30: Schematic overview of the momentum microscopy end station (from [28]) provided by KTH (Prof. Tjernberg).

mission measurements for catalysis and other science areas. The end station will be developed and commissioned by Stockholm University (Anders Nilsson and his designated successor Martin Beye) and will be based on a similar design as the Polaris end station [29] shown in Fig. 3.31.

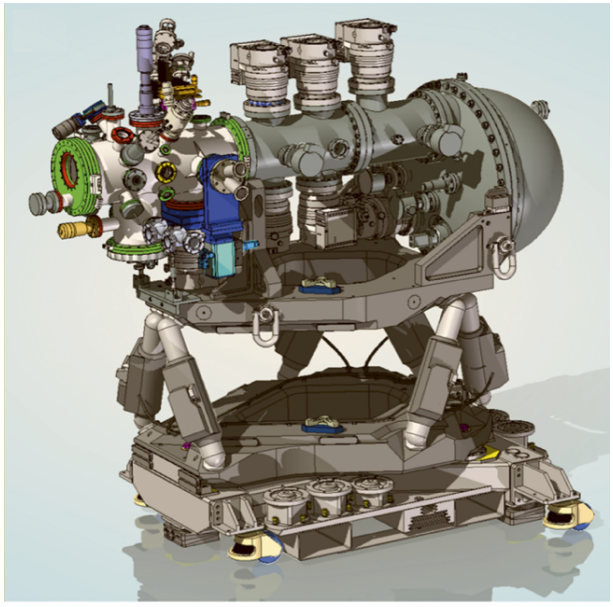

Figure 3.31: Schematic overview of the ambient-pressure photoemission end station (from [29]) provided by SU (Prof. Nilsson and his designated successor Dr. Beye).

3.7.2 Transient X-ray absorption spectroscopy

The envisioned setup for time-resolved tender to hard X-ray absorption spectroscopy will allow to measure in the transmission mode both thin solid-state samples and molecules in a liquid jet setup. Sample thickness can be of the order of 100 µm. The energy of the transmitted X-rays (broadband beam) will be analyzed behind the sample using a crystal-based X-ray spectrometer. In order to increase X-ray transmission and reduce X-ray scattering noise, the chamber will be constantly kept under a 500 mbar He atmosphere using a He pressure regulation system. The incident broadband X-ray beam with a bandwidth of 1% will impinge on the sample. A spectrometer behind the sample will be used to disperse and detect the transmitted intensities (the focusing optic in the beamline focuses the parallel beam onto the sample and a bent crystal analyzes the transmitted beam with a focus on the detector). This detection scheme will allow to measure full absorption-delay maps of 4d transition metal L-edges as well as sulfur and phosphorus K-edges at the lower end of the spectrum of the source (e.g. at 3 keV this covers a spectral range of 30 eV). At the higher end, the K-edges of 3d transition metals as well as L-edges of 5d transition metals will be accessible.

3.7.3 Resonant X-ray scattering

The X-ray diffraction and scattering experiments can be performed using an existing diffractometer at Uppsala University. It includes a two-circle Theta/2Theta goniometer with a detector arm rotatable in the horizontal plane for 2Theta measurements in a wide angular range. This allows aligning the detector at specific Bragg scattering angles or in transmission geometry. A 1-dimensional detector on the detector arm is positioned at a distance of $\sim$30 cm from the sample. In addition, rotation of the sample along the Chi and Phi angles, with rotational axes in the plane perpendicular to the X-ray beam, are permitted. The experiments will be performed at photon energies $>$6 keV, thus avoiding vacuum conditions. A lead-based radiation protection enclosure will surround the experiment station.

The diffractometer combined with the X-ray beam from the Ångström laser and a femtosecond optical pump laser facilitates studies of lattice dynamics. The X-ray flux of the broadband beamline (see Table 1) is at least comparable to that of laboratory-based rotating anode sources. This enables time-resolved measurements on samples that have been characterized with X-rays in the home laboratories. The distinct advantage will be the tunable X-ray energy of the Ångström Laser enabling resonant X-rays scattering measurements. In addition, the X-ray output is also partially coherent. The small X-ray beam size at the source (3.5 µm RMS) implies a significant transverse coherence can be produced with the Ångström laser [30]. We estimate a coherent-flux fraction with respect to the total flux $> 10^{-4}$ at 6 keV. Together with event-based single-photon 2D detection of scattered X-rays [31] this may allow performing at least proof-of-principle experiments already for the Ångström Laser baseline design. However, we expect that such coherent scattering and possibly imaging experiments will become more common once the Ångström Laser is upgraded to fully coherent output (see section 3.10).

3.8 Timing and synchronization

Synchronization between the generated X-ray pulses and those produced by external lasers is crucial for pump-probe experiments. In such measurements a synchronization level below the X-ray-pulse duration is typically desired in order to avoid a significant influence of the timing jitter between the pump and probe pulses on the temporal resolution. The total timing jitter originates from the arrival-time fluctuations of both the electron-bunches and the external-laser pulses. Thus, efficient jitter reduction requires synchronization of several sub-systems including cathode gun, accelerator components, RF field and external lasers. Synchronization

of the different sub-systems is achieved by distributing a high-quality reference signal produced by the master oscillator.

The proposed accelerator design is based on superconducting accelerator technology, which promotes a low temporal jitter of the electron-bunches. Superconducting technology enables operation with constantly powered accelerator cavities and therefore a more stable condition for electron acceleration is achieved. Beam stability is also supported by the lack of chicanes in the baseline design of the linac, which converts unavoidable RF phase and amplitude noise into substantial timing fluctuations.

A schematic of the envisioned Ångström Laser timing and synchronization system is shown in Fig. 3.32. The reference clock is the Photonics Microwave Generator (PMWG), model PMWG-1500 of MenloSystems GmbH. PMWG implements the phase-coherent division of the optical comb to provide the frequency reference for the microwave carrier at 1.3 GHz. The technology significantly outperforms commercially available microwave oscillators in terms of frequency stability. The RF distribution system is designed to be electronic owing to the relative compactness of the Ångström Laser. The RF-field stabilization is controlled with a Low-Level RF (LLRF) system. Such a system, developed for the free-electron laser in Hamburg, FLASH, provides 100-fs level stabilization of the electron-bunch arrival time [32]. Beam arrival-time monitors with few-fs precision combined with feedback loops can be employed to reduce the electron-bunch arrival-time jitter to well below 100 fs if necessary [33]. However, given the expected stable conditions for the e-beam and the 200 fs duration of the X-ray pulse, stabilization of the RF cavity field should be sufficient for controlling the electron bunch jitter in the baseline design. The envisioned TDC electron-bunch arrival-time diagnostics for the Ångström Laser permits parasitic monitoring of the timing between the electron-bunches and the RF-field. The RF-field is, in turn, synchronized with the optical laser pulses via the PMWG reference clock at a 20 fs RMS synchronization level (see below). In the absence of X-ray arrival time diagnostics due to limited X-ray flux of the ICS, the TDC therefore provides an important monitor of the optical laser-pulse and electron-bunch synchronization with sub-100 fs precision.

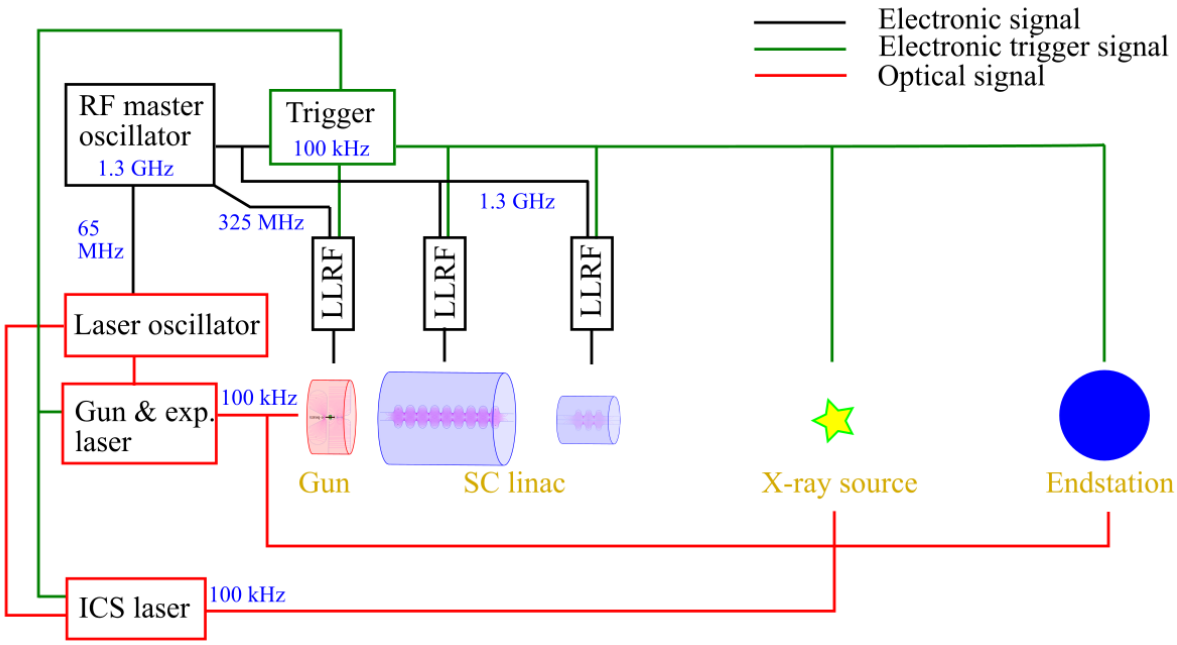

Figure 3.32: Schematic overview of the Ångström Laser timing and synchronization.

All the laser sources are synchronized to the PMWG reference clock and e-beam via an external optical oscillator. The laser synchronization is schematically shown in Fig. 3.33. The

highly stable oscillator, FLINT model of Light Conversion UAB, is locked to the RF frequency clock via a phase-locked loop (PLL) provided by the Balanced Optical Phase Detector (BOPD) of Cycle GmbH. BOPD generates a baseband signal that is proportional to the timing error between the two inputs. This signal is used to adjust the FLINT cavity length and control its pulse repetition rate (PRR) which is set to 65 MHz. BOPD is immune to amplitude fluctuations in both optical and microwave channels and allows to reach microwave-to-optical synchronization with a time jitter of down to 20 fs RMS. An optical pulse train produced by the FLINT oscillator is used to synchronize the CARBIDE power amplifier with the TRUMPF TruMicro 2000 laser via an optical fiber link. Possible time lag between the laser pulses arising due to temperature drift and mechanical vibrations over the laser beam paths, both during the amplification stages of the inverse Compton source (ICS) laser and beam transportation, are compensated by optical delay lines linked to a feedback system. The system includes the Balanced Optical Cross Correlator (BOC) of Cycle GmbH and allows to control time jitter down to 10 fs RMS. Synchronization levels on the order of 30 fs RMS has been demonstrated using a similar system at the Arizona compact X-ray light source [34].

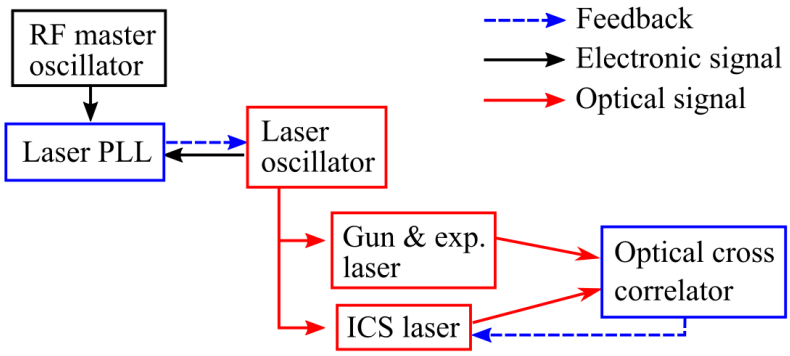

Figure 3.33: Schematic of the laser synchronization.

The trigger distribution of the Ångström Laser is shown by the green lines in Fig. 3.32. The trigger is required for timing of both machine subsystems and those connected with experiments at the 100 kHz repetition rate. Examples of systems requiring timing trigger input at the experimental stations are detectors, data acquisition and sources of external stimuli such as magnetic fields. In addition, diagnostics in all parts of the Ångström Laser will demand trigger input.

3.9 Layout of the Ångström Laser

The FREIA Laboratory at the Department of Physics and Astronomy of Uppsala University is well equipped to host and operate the superconducting accelerator for the Ångström Laser X-ray source. The FREIA Laboratory of around 1 000 m^2 is dedicated to (high-power) characterization of superconducting cavities and superconducting magnets. It houses a cryogenic system with a He liquefier, several high-power RF sources at 325 MHz, a horizontal and a vertical cryostat, and electronics for stabilizing accelerating fields in superconducting cavities. This is the typical infrastructure required for a superconducting accelerator. Figure 3.34 shows the area potentially available for the X-ray source along with a preliminary layout of technical systems of the X-ray source. This area contains 3 existing concrete bunkers which can be reconfigured to accommodate the Ångström Laser. An existing laser laboratory will house the femtosecond drive laser (optical undulator) and the pump lasers (for electronic excitation of samples and triggering of fast processes) while the experiment will be performed from a cen-

tral control room. In Fig. 3.34 the baseline design of the Ångström Laser (blue) is presented together with a possible future upgrade (yellow), (see also section 3.10).

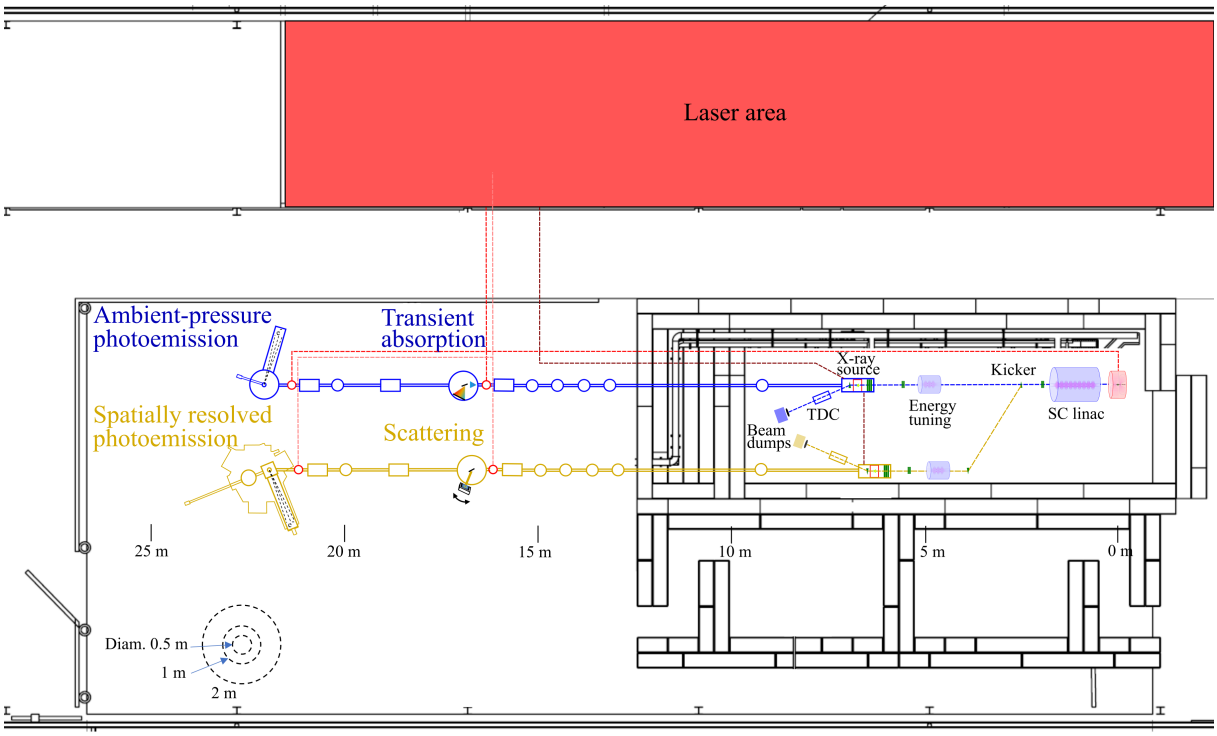

Figure 3.34: Layout of the Ångström laser at the FREIA laboratory. Blue color indicates the baseline design of the electron and photon beamlines and end stations, yellow shows the upgrade possibility of an electron bunch compressor with a connected X-ray beamline. A kicker magnet will enable operating both beamlines simultaneously at 100 kHz repetition rate each. The X-ray-beamline components are to scale.

3.10 Upgrade possibilities

The baseline design of the Ångström Laser described in detail in this study is illustrated schematically in Fig 3.34 (outlined in blue). Below we describe several possibilities towards improving and upgrading the X-ray source characteristics.

Initial **operational improvements** of the Ångström Laser will be geared towards better understanding and controlling the parameters leading to X-ray emission, i.e. the efficiency of the coupling between optical undulator and the electron bunch. Parameters such as shaping of the electron bunch and its interaction with the laser light, as well as the shaping of the injector laser profile clearly are important. In addition, we will explore the possibility of generating polarized X-rays by modifying the polarization of the optical undulator. While polarization changes from horizontal to vertical polarization are straightforward, it is also possible to imprint circular polarization onto the emitted X-rays [35, 36]. These source improvements will go hand-in-hand with the continuous buildup of the experimental infrastructure.

Following the demonstration of successful operation, it will be straightforward to upgrade the Ångström Laser for **increased user capacity**. This is schematically depicted in Fig. 3.34 (outlined in yellow). The photoinjector is capable of 200 kHz operation. Every second electron bunch will then be magnetically kicked down the second yellow branchline and generates X-rays via interaction with the same laser pulses that have already been used for the blue branchline

in Fig. 3.34. This allows simultaneous operation of two beamlines each with 100 kHz repetition rate. The X-ray beam energies can be independently varied by positioning a second energy tuning cavity module (see Fig. 3.3) in the yellow branchline. It enables, for instance, the simultaneous independent operation of the two photoemission end stations described in section 3.7.1. The additional cost for such an upgrade would mainly be the additional kicker magnets, a second energy tuning cavity, a second beamline, and additional pump laser capabilities for the end stations. We note that such a second branchline can also include electron bunch compression capabilities. The electron bunch compressor would enable short X-ray pulses down to about 10 fs.

Further upgrades of the Ångström Laser can enable a fully **coherent X-ray output** over an extended X-ray energy range and with a photon flux several orders of magnitude higher. These coherent X-ray generation schemes are currently being tested at the compact X-ray free-electron laser facility at Arizona State University [37, 38, 39] and at the Center for Quantum Materials and Technology at Eindhoven University of Technology [40, 41].

3.11 Radiation safety

The electron accelerator will be contained in a concrete bunker, which provides the required shielding of any radiation produced by the electron beam. Entrance to the bunker will be controlled by interlocked access doors. Within the bunker electron-beam dumps of concrete blocks will stop electrons that have been extracted by a dipole magnet, e.g., after the interaction point with the laser beam. The locations of the beam dumps are shown in Fig. 3.34. Interlock systems acting via beam shutters, triggers or breaking of the power, depending on the situation, will ensure radiation protection in case of failure of any component.

The X-ray beams will be transported in vacuum pipes and experiments will typically be performed in vacuum experimental stations, which provide sufficient radiation protection. In specific exceptions where experiments are not performed in vacuum stations, suitable radiation protection enclosures will be built.

Entrance to the optical laser rooms will be controlled by interlock access doors.

3.12 Data infrastructure

Control systems

The FREIA laboratory is presently using the EPICS control system, which is a common software at accelerator facilities. All systems running at FREIA, such as LLRF, interlocks and radiation monitors, are connected to EPICS. This control system will also be suitable for the Ångström Laser and is planned to be adapted to include all components of the new facility. Components that have to be controlled include magnets, vacuum, lasers, synchronization tools, interlocks and diagnostics. Devices will be integrated using EPICS-based interfaces that permit connection with PLCs (Programmable Logic Controllers) or computers for specific control close to the device.

Data acquisition

The data acquisition (DAQ) system enables efficient acquisition, storage and processing of generated data. The demands of the DAQ are determined by the properties of the source, detectors, data-analysis algorithms and the requirements for fast feedback to users in real time. Several types of detectors must be supported by the DAQ for the Ångström Laser, e.g., various CCD cameras, electron time-of-flight detectors and diodes. The data infrastructure will provide

fast DAQ and online processing of data using shared computer clusters. The acquired data can be stored in online FLASH-based storage and will subsequently be transferred to a larger offline storage, which will be accessed by a computer cluster. The data format is envisioned to be HDF5, which is compatible with the international community's standard.

R&D and operational aspects of the Ångström Laser

4.1 Governance and operation

Figure 4.1 illustrates the organizational structure of the Ångström Laser. The Facility will be physically located at the FREIA Laboratory (see Fig. 3.34) of the Department of Physics and Astronomy at Uppsala University. The FREIA Laboratory is Sweden's center for cryogenic accelerator R&D. FREIA is operating infrastructure for Helium liquefication and high-power RF electronics which will also be used for the Ångström Laser. Leveraging the expertise at FREIA and the Department of Physics and Astronomy will enable us to support the operation of the Ångström Laser. The anticipated annual operational budget of the Ångström Laser will be covered via the FREIA Laboratory by the Department of Physics and Astronomy.

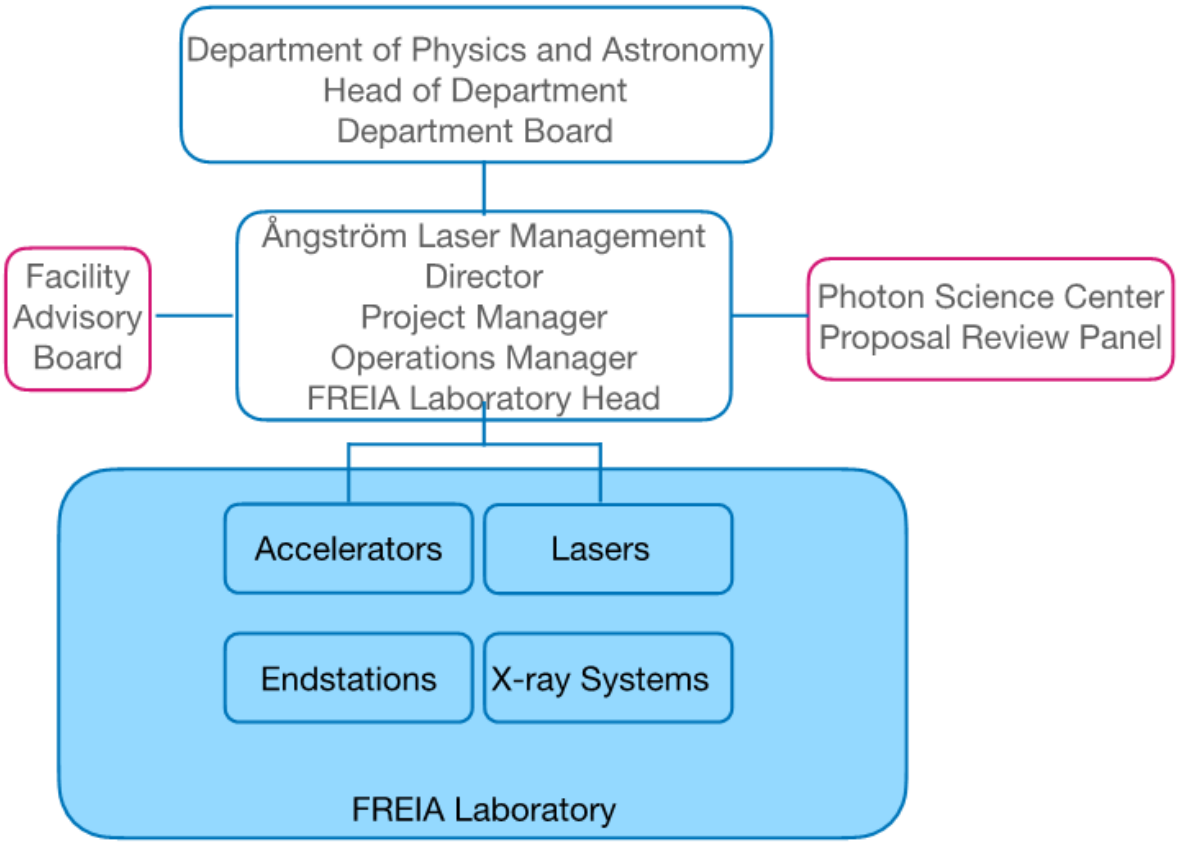

Figure 4.1: Governance structure of the Ångström Laser.

The Ångström Laser management team consisting of a director, project manager, operations manager and the FREIA Laboratory Head will report to the Department of Physics and Astronomy represented by the Department Head and the Department Board. A Facility Advisory Board will provide guidance in strategically positioning the Ångström Laser interna-

tionally (see Figs. 1.1 and 1.2) and growing a sustainable user community. We plan to attract international experts in the relevant fields. The cross disciplinary expertise of the Uppsala University Photon Science Center will be important for embedding a medium-scale facility into the Uppsala and national science landscape.

User access to the Ångström Laser will be based on scientific quality. We plan to engage the Uppsala University Photon Science Center to select experts in the field for a proposal review panel that will assess proposals submitted twice a year. Access will be without access fees. In addition to standard user proposals, we will explore new ways of access enabled by the unique position of the Ångström Laser in the middle of a university campus.

4.2 Timeline

The project is organized in the form of Work Packages (WP) and the high-level Gantt chart for the project is shown in Fig. 4.2. Specifically, it depicts main tasks, milestones showing the completion of major steps and deliverables in the form of commissioned systems. The schedule is tight and demanding. Its realization will be achieved via a detailed planning within **WP 1**.

In **WP 1** during the 1st year we will focus on complementing the FREIA team in certain areas of competence, including the expertise required for the Ångström Laser (see Table **??**) and develop a detailed plan for resource prioritization, a schedule for procurements, further investigate possible risks for the project and develop mitigation strategies that also address the risks of higher costs. In parallel, we will start a detailed technical design study (TDR) that will naturally launch the other WPs dedicated to research & development (R&D) of the required systems of the Ångström Laser.

The **WP 2** is largely devoted to the coordination between projects at the FREIA Laboratory in order to ensure the proper timing and allocation of the resources where and when they are needed. We foresee a reconstruction of the FREIA Laboratory, possibly even enlarging the FREIA building. The construction company, Akademiska Hus, will be sub-contracted to suggest a technical solution and give a cost estimate. Inside the FREIA Laboratory, we plan to relocate ongoing projects to free up space for two planned large-scale projects: the Ångström Laser and the testing of superconducting cryomodules for MYRRHA (https://myrrha.be) – “the world’s first large scale Åccelerator Driven System that consists of a subcritical nuclear reactor driven by a high-power linear accelerator”. Also, the FREIA Laboratory will be prepared for hosting the 5-kW optical undulator laser system with a footprint of around 1.5x9 m^2. A clean-room type environment with temperature and humidity control will be established either by expanding the present laser room or by building a new one.

The completion of the design and the construction of the electron injector is the main task of **WP 3**. The present physics design will be complemented with an engineering design of RF parts, a thermal analysis and the design of vacuum and mechanical parts. After cross-checking our design with colleagues from other laboratories (a process described as “expert cross-check” in Fig. 4.2), material and components will be procured and the injector will be fabricated in-house using the very experienced mechanical workshop at Uppsala University. There is significant synergy between the Ångström Laser project and the Uppsala University mechanical workshop via the construction of complex mechanical systems that help maintaining high-class mechanical engineers and by training junior colleagues. Developing the electron beam diagnostics will ensure that the design specifications are met at each step. Overall, **WP 3** requires a large amount of in-house R&D.

The superconducting accelerator development in **WP 4** largely uses accelerator compo-

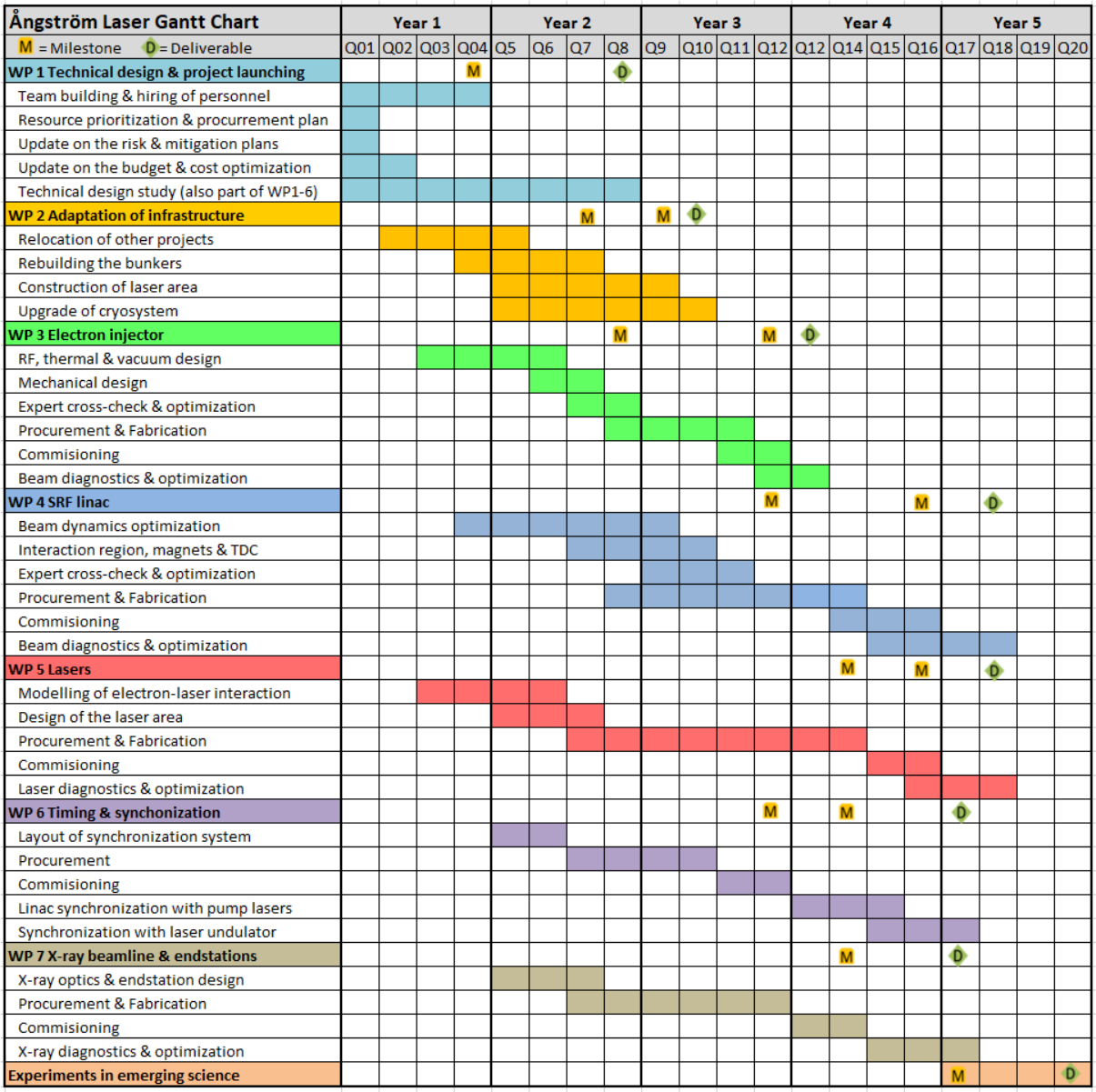

Figure 4.2: Timeline of major installation and commissioning steps.

nents that will be ordered from industry. The major components are the two superconducting cavities, which are available off-the-shelf items, and two cryomodules, which must be first designed to meet our requirements on space and mechanical stability. The magnets used in the project are not standard because of stringent constraints on their size and magnetic field strength and will be designed in-house. The production of the magnets can be done by Swedish companies such as Scandinova with whom we have a long-standing collaboration. The commissioning of the superconducting accelerator is closely related to the commissioning of the injector and the beam diagnostics and will start after the electron beam from the injector is fully characterized and controlled.

WP 5 is devoted to laser systems such as the laser undulator and a set of pump lasers for pump-probe experiments. The laser undulator will make use of a 5 kW laser system based on thin-disk technology, which became mature in recent years. Industrial-grade 1 kW laser systems are available off-the-shelf. A system delivering 95 mJ pulses at 20 kHz (1.9 kW) was demonstrated in 2021 and is available with a special order. The required 5 kW laser system

will be designed and built specifically for this project. We contacted major laser companies in Europe (thin-disk technology was developed primarily by European companies) and they are willing to collaborate to deliver an efficient solution. Femtosecond laser systems for pump-probe experiments are already available at FREIA and based on an 80-W Carbide laser from LightConversion.

The critical task of synchronization and achieving spatial overlap of electron bunches and laser pulses is tackled in **WP 6**. During the present conceptual design study and also the one for the Soft X-ray Laser at MAX IV (Lund, Sweden) we have gained a comprehensive overview of different synchronization schemes and established contacts with the laboratories having relevant experience. The challenges are similar to those for seeding free electron lasers and we will collaborate with scientists from FERMI in Trieste, currently the only seeded FEL in operation. We expect to also benefit from the operational experience gathered at linac-based inverse Compton facilities (TU Eindhoven and Arizona State University). Even though the complexity of **WP 6** is very high, we do not expect major risks and envision building a small test stand with the existing laser system and a femtosecond DC electron gun in order to have the synchronization and overlap system ready for use when the superconducting accelerator will be commissioned. However, we are aware that the optimization of the inverse Compton process will continue after the Ångström Laser has started operation as outlined in section 3.10.

WP 7 is devoted to X-ray beamline and end stations. Beamline development has its own challenges due to the relatively large divergence of X-ray radiation from the inverse Compton source. However, no major risks are foreseen as we have extensive experience that includes the complete design and construction of the Veritas X-ray beamline at MAX IV as well as spectrometers for the European XFEL and various in-house and facility-based end stations.

The possible risks inherent to the different WPs and their mitigations are discussed further in section 4.4.

4.3 Personnel

Table 4.1 summarizes the competences needed for the project. In green is shown the competence already available for the project; in yellow, the competence that must be expended; and in red are shown areas where additional personnel must be hired or “loaned” from partner laboratories. A plan for hiring and carrier development will be set at the beginning of the project and is part of WP 1.

4.4 Risk assessment

Table 4.2 summarizes the identified risks involved in the work packages of Fig. 4.2 and their mitigation strategies. The 2nd column describes possible risks whereas the 3rd column assesses the risk level and main impact on the project (time delay or extra cost). The last column lists suggested mitigation measures. From our experience with large scale projects, contingency funding (typically 20%) must be foreseen in the case the mentioned risks realize in practice despite mitigation measures. Very broadly risks can be divided into 2 categories: (1) failure or multifunctioning of equipment and (2) extra cost due to personnel such as competent colleagues leaving the project for various reasons and new people must be hired and educated. *Though the contingency funding is not a must requirement and not included into the budget, a plan for covering the cost of potential risks must be in place before the project starts.*

Table 4.1: Major competences required for the project: green implies that the competence is already available, yellow – competence partially available, red - competence is needed.

	Required competences
1.	Coordination and Leadership
2.	System integration
3.	Site manager
4.	Avdelningföreståndare
5.	Scientist - laser physicist
6.	Scientist - laser physicist
7.	Scientist - e-gun R&D
8.	Engineer - e-gun hardware
9.	Scientists - linac R&D
10.	Engineer - linac hardware
11.	Scientist - beam diagnostics
12.	Engineer - magnets & vacuum
13.	Scientist - SC RF
14.	Engineer - cryosystem
15.	Engineer - synchronization
16.	Engineer - mechanical design & installation
17.	Scientist - X-ray beamline
18.	Scientist - end station
19.	Scientist - laser-electron interation
20.	Senior expert consultant

Table 4.2: Identified risks, their likelihood and impact on the project, and proposed mitigation measures.

	Description of the risk	**Risk level/ impact on project**	**WP**	**Mitigation measure/ Comment**
1.	There is an acute shortage of qualified personnel in the fields of accelerators and FELs in Europe because many young and senior specialists leave for American National laboratories.	High/Delay	1	Hire early-career specialists and invite senior colleagues from other laboratories to participate in the project and supervise junior colleagues. Uppsala and Lund universities have academic programs in accelerator physics & instrumentation so early-career specialists can be fostered internally. We have good connections to the UK (Daresbury & Cockcroft Institute), which can be also a significant resource of specialists. DESY and PITZ (Germany) are other sources of qualified specialists.

2.	Insufficient space at the FREIA Laboratory to host the Ångström Laser project and operate simultaneously other large projects such as testing of cryomodules.	Medium/ Extra cost	1	The FREIA Laboratory can be extended by building a laser laboratory next to it. The second floor of FREIA, currently used for offices, can be modified to host a control room and additional equipment such as LLRF and control systems, a data acquisition system.
3.	Increased cost of the project in view of the inflation and higher cost of personnel.	Medium/ Extra cost	1	Closely investigate the possibility of reusing existing equipment from partner laboratories. Establish knowledge exchange programs with partner laboratories with shared cost of the personnel. Use EU funding opportunities to host PhD students and postdocs.
4.	Insufficient cryogenic capacity for operating two large projects simultaneously because of space and funding limitations.	Medium/ Extra cost	2	Potential delay of the commissioning of the superconducting linac up to 6 months.
5.	Competition for personal and infrastructure access among several projects.	High/ Delay	2	Set up a plan to "borrow" personnel and equipment from other laboratories during peak workloads.
6.	Excessively high reconstruction cost by Akademiska Hus.	High/ Extra cost	2	Avoid reconstructions that will increase the rent.
7.	Other laboratories cannot share and explain their blueprints of mechanical parts for the gun and other components.	Medium/ Delay	3	Potential delay of the project because in-house engineers will need more time to go through mechanical drawing and probably design some parts from scratch.
8.	The nominal accelerating gradient is not reached in time because of RF breakdowns, dark currents or multipacting.	High/ Extra cost	3	The required RF field strength was demonstrated in other design. In the worst-case scenario, an additional normal-conducting booster can be installed.
9.	Delay of the injector components.	Medium/ Delay	3	The assembly is planned in-house and backup options for alternative solutions will be prepared.

10.	Beam emittance does not reach the nominal design value.	Medium / Delay	3	A solution for cathode replacement and laser cleaning will be implemented from the project start.
11.	Misalignment of the mechanical and electric axes of the cavities.	Low/ Extra cost	3	The cavities are large and the relative accuracy is expected to be high.
12.	Insufficient quality of the electrical connection between the cathode assembly, the gun cavity and booster cavity.	Medium/ Extra cost	3	A scaled compact version of the photoinjector will be fabricated and tested in an RF lab.
13.	Risk of not achieving the nominal accelerating gradient in the TESLA cavity.	Low/ Delay	4	The required accelerating gradient of 20.25 MV/m was routinely achieved at the European XFEL.
14.	Major delay of cryomodules because of a high demand and technical challenges.	High/ Delay	4	The existing FREIA cryomodule can be used as a temporary solution to host SC cavities.
15.	Insufficient compression of electron bunches.	Low/ Extra cost	4	Present simulations show bunch compression down to 100 fs FWHM and a robust operation regime.
16.	Contamination of SC cavities during installation.	Low/ Extra cost	4	The FREIA team has tested over 30 SC cavities and has the required experience.
17.	Long-term fluctuations of laser parameters.	Low/ Extra cost	5	The laser will be installed in a clean room with temperature and humidity control.
18.	Risk of not achieving the nominal laser parameters.	Low/ Delay	5	According to the design, there is enough margin at each amplification stage.
19.	Delay of the laser system.	Low/ Delay	5	The laser system will be built by several companies, which allows for re-distributing the workload if needed.
20.	Low accuracy of the transverse alignment of laser and electron beams.	High/ Extra cost	6	While building the main system, we will set up a test bench for training using an existing laser and a simple DC photogun. All electronics and software will be tested before the main part of the project starts.
21.	Insufficient synchronization accuracy.	Low/ Extra cost	6	The first stage synchronization accuracy of 100 fs has been demonstrated in many laboratories and proven commercial solutions are available.

22.	The X-ray beamline does not meet the requirements.	Low/ Extra cost	7	There is broad in-house experience in designing and building X-ray beamlines and components.
23.	Delay of X-ray optics components.	Low/ Extra cost	7	Major R&D will take place in-house with a good control of risks and timing.
24.	Insufficient accuracy of X-ray and electron beam diagnostics.	Low/ Extra cost	7	Multiple diagnostics schemes are planned for increased accuracy and reliability.
25.	Personnel safety.	Low/ Extra cost	7	Personnel safety is of the utmost importance and safety procedures will be implemented from the day one and regularly revised and updated.

Table 4.3 presents a risk assessment matrix and shows the impact of a risk versus its likelihood.

Table 4.3: Risk matrix. The numbers in the cells refer to the risks presented in Table 4.2.

Risk likelihood	Impact of the risk		
	Minor	Moderate	Major
High	14	6,8,10	1,5
Medium	11,12	2,7,9,10	3,4
Low	13	15-17,22,23	18-21,24,25

References

Chapter 1

[1] Tenio Popmintchev et al. “Bright coherent ultrahigh harmonics in the kev x-ray regime from mid-infrared femtosecond lasers”. In: *Science* 336.6086 (June 2012), pp. 1287–1291. ISSN: 10959203. DOI: 10.1126/science.1218497. URL: www.sciencemag.org.

[2] Lou Barreau et al. “Efficient table-top dual-wavelength beamline for ultrafast transient absorption spectroscopy in the soft X-ray region”. en. In: *Sci. Rep.* 10.1 (Apr. 2020), p. 5773.

[3] D. E. Rivas et al. “Propagation-enhanced generation of intense high-harmonic continua in the 100-eV spectral region”. In: *Optica* 5.10 (Oct. 2018), pp. 1283–1289. DOI: 10.1364/OPTICA.5.001283. URL: https://opg.optica.org/optica/abstract.cfm?URI=optica-5-10-1283.

[4] Yoann Pertot et al. “Time-resolved x-ray absorption spectroscopy with a water window high-harmonic source”. en. In: *Science* 355.6322 (Jan. 2017), pp. 264–267.

[5] F. Campi et al. “The high intensity HHG beamline at Lund Laser”. In: *Research in Optical Sciences*. Optica Publishing Group, 2014, HW3C.1. DOI: 10.1364/HILAS.2014.HW3C.1. URL: https://opg.optica.org/abstract.cfm?URI=HILAS-2014-HW3C.1.

[6] Vlad Musat, Andrea Latina, and Gerardo D’Auria. “A high-energy and high-intensity inverse Compton scattering source based on CompactLight technology”. en. In: *Photonics* 9.5 (Apr. 2022), p. 308.

[7] *CXFEL: Compact X-ray free electron laser*. URL: https://biodesign.asu.edu/cxfel/.

[8] *Kai Siegbahn, Nobel Prize lecture (1981)*. URL: https://www.nobelprize.org/prizes/physics/1981/siegbahn/lecture/.

[9] Regine Gradl et al. “Propagation-based phase-contrast X-ray imaging at a compact light source”. en. In: *Sci. Rep.* 7.1 (July 2017), p. 4908.

[10] *SmartLight*. URL: https://research.tue.nl/en/impacts/smartlight.

[11] *ASU CXFEL*. URL: https://biodesign.asu.edu/cxfel/.

[12] Niko Pontius et al. “The FemtoSpeX facility at BESSY II”. In: *J. Large-scale Res. Facil. JLSRF* 2.A46 (Feb. 2016).

[13] C Stamm et al. “Femtosecond modification of electron localization and transfer of angular momentum in nickel”. en. In: *Nat. Mater.* 6.10 (Oct. 2007), pp. 740–743.

Chapter 2

[1] Zhi Wei Seh et al. “Combining theory and experiment in electrocatalysis: Insights into materials design”. en. In: *Science* 355.6321 (Jan. 2017), eaad4998.

[2] Peter Amann et al. “The state of zinc in methanol synthesis over a Zn/ZnO/Cu(211) model catalyst”. en. In: *Science* 376.6593 (May 2022), pp. 603–608.

[3] A Nilsson et al. “Catalysis in real time using X-ray lasers”. en. In: *Chem. Phys. Lett.* 675 (May 2017), pp. 145–173.

[4] Leif Hammarström. “Accumulative charge separation for solar fuels production: coupling light-induced single electron transfer to multielectron catalysis”. en. In: *Acc. Chem. Res.* 48.3 (Mar. 2015), pp. 840–850.

[5] Nathan S Lewis and Daniel G Nocera. “Powering the planet: chemical challenges in solar energy utilization”. en. In: *Proc. Natl. Acad. Sci. U. S. A.* 103.43 (Oct. 2006), pp. 15729–15735.

[6] Wolfgang Lubitz, Edward J Reijerse, and Johannes Messinger. “Solar water-splitting into H2 and O2: design principles of photosystem II and hydrogenases”. en. In: *Energy Environ. Sci.* 1.1 (2008), p. 15.

[7] None None and Basic Energy Sciences Roundtable. *Report of the basic energy sciences roundtable on liquid solar fuels*. Tech. rep. DOESC Office of Basic Energy Sciences, Apr. 2019.

[8] Phebe Asantewaa Owusu and Samuel Asumadu-Sarkodie. “A review of renewable energy sources, sustainability issues and climate change mitigation”. en. In: *Cogent Eng.* 3.1 (Dec. 2016), p. 1167990.

[9] *International Energy Agency, ”World Energy Outlook 2021”*. URL: https://www.iea.org/reports/world-energy-outlook-2021.

[10] Tamara Sloboda et al. “A method for studying pico to microsecond time-resolved core-level spectroscopy used to investigate electron dynamics in quantum dots”. en. In: *Sci. Rep.* 10.1 (Dec. 2020), p. 22438.

[11] M B de la Mora et al. “Materials for downconversion in solar cells: Perspectives and challenges”. en. In: *Sol. Energy Mater. Sol. Cells* 165 (June 2017), pp. 59–71.

[12] Alexander J Baldacchino et al. “Singlet fission photovoltaics: Progress and promising pathways”. en. In: *Chem. Phys. Rev.* 3.2 (June 2022), p. 021304.

[13] J M Serra et al. “Hydrogen production via microwave-induced water splitting at low temperature”. en. In: *Nat. Energy* 5.11 (Nov. 2020), pp. 910–919.

[14] Charles C L McCrory et al. “Benchmarking hydrogen evolving reaction and oxygen evolving reaction electrocatalysts for solar water splitting devices”. en. In: *J. Am. Chem. Soc.* 137.13 (Apr. 2015), pp. 4347–4357.

[15] Vincent Maurice and Philippe Marcus. “Progress in corrosion science at atomic and nanometric scales”. en. In: *Prog. Mater. Sci.* 95 (June 2018), pp. 132–171.

[16] Tobias Binninger et al. “Thermodynamic explanation of the universal correlation between oxygen evolution activity and corrosion of oxide catalysts”. en. In: *Sci. Rep.* 5.1 (July 2015), p. 12167.

[17] O Barrera et al. “Understanding and mitigating hydrogen embrittlement of steels: a review of experimental, modelling and design progress from atomistic to continuum”. en. In: *J. Mater. Sci.* 53.9 (Feb. 2018), pp. 6251–6290.

[18] J Soltis. “Passivity breakdown, pit initiation and propagation of pits in metallic materials – Review”. en. In: *Corros. Sci.* 90 (Jan. 2015), pp. 5–22.

[19] None None. *Basic energy sciences roundtable: Foundational science for carbon-neutral hydrogen technologies*. Tech. rep. Oct. 2021.

[20] Andreas Blomqvist et al. “Significance of self-trapping on hydrogen diffusion”. en. In: *Phys. Rev. Lett.* 105.18 (Oct. 2010), p. 185901.

[21] H Metzger, J Peisl, and J Wanagel. “Huang diffuse scattering of X-rays from the displacement field of hydrogen in niobium”. In: *J. Phys.* 6.12 (Dec. 1976), pp. 2195–2206.

[22] Cem Örnek et al. “Operando time- and space-resolved high-energy X-ray diffraction measurement to understand hydrogen-microstructure interactions in duplex stainless steel”. In: *Corrosion Science* 175 (2020), p. 108899. ISSN: 0010-938X. DOI: https://doi.org/10.1016/j.corsci.2020.108899. URL: https://www.sciencedirect.com/science/article/pii/S0010938X20313032.

[23] Cem Örnek et al. “Metastable precursor structures in hydrogen-infused super duplex stainless steel microstructure – An operando diffraction experiment”. In: *Corrosion Science* 176 (2020), p. 109021. ISSN: 0010-938X. DOI: https://doi.org/10.1016/j.corsci.2020.109021. URL: https://www.sciencedirect.com/science/article/pii/S0010938X2031180X.

[24] Cem Örnek et al. “Time-resolved grazing-incidence X-ray diffraction measurement to understand the effect of hydrogen on surface strain development in super duplex stainless steel”. en. In: *Scr. Mater.* 187 (Oct. 2020), pp. 63–67.
[25] *Quantum Materials for Energy Relevant Technology*. URL: https://today.lbl.gov/2016/12/21/doe-report-on-quantum-materials-for-energy-relevant-technology-now-available/.
[26] L Stojchevska et al. “Ultrafast switching to a stable hidden quantum state in an electronic crystal”. en. In: *Science* 344.6180 (Apr. 2014), pp. 177–180.
[27] Edbert J Sie et al. “An ultrafast symmetry switch in a Weyl semimetal”. en. In: *Nature* 565.7737 (Jan. 2019), pp. 61–66.
[28] D Fausti et al. “Light-induced superconductivity in a stripe-ordered cuprate”. en. In: *Science* 331.6014 (Jan. 2011), pp. 189–191.
[29] D Kutnyakhov et al. “Time- and momentum-resolved photoemission studies using time-of-flight momentum microscopy at a free-electron laser”. en. In: *Rev. Sci. Instrum.* 91.1 (Jan. 2020), p. 013109.
[30] Michael Heber et al. “Multispectral time-resolved energy-momentum microscopy using high-harmonic extreme ultraviolet radiation”. en. In: *Rev. Sci. Instrum.* 93.8 (Aug. 2022), p. 083905.
[31] Albert Fert, Vincent Cros, and João Sampaio. “Skyrmions on the track”. en. In: *Nat. Nanotechnol.* 8.3 (Mar. 2013), pp. 152–156.
[32] Stuart S P Parkin, Masamitsu Hayashi, and Luc Thomas. “Magnetic domain-wall racetrack memory”. en. In: *Science* 320.5873 (Apr. 2008), pp. 190–194.
[33] Felix Büttner et al. “Observation of fluctuation-mediated picosecond nucleation of a topological phase”. en. In: *Nat. Mater.* 20.1 (Jan. 2021), pp. 30–37.
[34] Diego Turenne et al. “Nonequilibrium sub-10 nm spin-wave soliton formation in FePt nanoparticles”. en. In: *Sci. Adv.* 8.13 (Apr. 2022), eabn0523.

Chapter 3

[1] R. P. Wells et al. “Mechanical design and fabrication of the VHF-gun, the Berkeley normal-conducting continuous-wave high-brightness electron source”. In: *Review of Scientific Instruments* 87.2 (Feb. 2016), p. 023302. DOI: 10.1063/1.4941836. URL: https://doi.org/10.1063/1.4941836.
[2] *ASTRA: A Space Charge Tracking Algorithm.* URL: https://www.desy.de/~mpyflo.
[3] *SLAC fires up electron gun for LCLS-II X-ray laser upgrade*. URL: https://www6.slac.stanford.edu/news/2019-05-30-slac-fires-electron-gun-lcls-ii-x-ray-laser-upgrade.
[4] *Berkeley Lab Delivers Injector That Will Drive X-Ray Laser Upgrade*. URL: https://newscenter.lbl.gov/2018/01/22/injector-gun-xray-laser-upgrade/.
[5] Anatoliy Opanasenko et al. “Nanometre-scale emittance beams from a continuous-wave RF gun”. In: (May 2021). arXiv: 2105.07923 [physics.acc-ph].
[6] Georgii Shamuilov et al. “Emittance self-compensation in blow-out mode”. In: *New J. Phys.* 24.12 (Dec. 2022), p. 123008.
[7] Clara J Saraceno et al. “The amazing progress of high-power ultrafast thin-disk lasers”. en. In: *J. Eur. Opt. Soc. Rapid Publ.* 15.1 (Dec. 2019).
[8] J K Lim et al. “Adjustable, short focal length permanent-magnet quadrupole based electron beam final focus system”. en. In: *Phys. Rev. Spec. Top. - Accel. Beams* 8.7 (July 2005).
[9] Georgia Paraskaki. “Free Electron Lasers (FELs): Bunch Compressor Design for X-FEL & Improvement of DFS algorithm for the FERMI FEL Free Electron Lasers”. PhD thesis. Sept. 2016.

[10] David Attwood and Anne Sakdinawat. *X-rays and extreme ultraviolet radiation*. 2nd ed. Cambridge, England: Cambridge University Press, Feb. 2017.
[11] Kwang-Jea Kim, Zhirong Huang, and Ryan Lindberg. *Synchrotron radiation and free-electron lasers*. Cambridge, England: Cambridge University Press, Apr. 2017.
[12] Winthrop J Brown and Frederic V Hartemann. "Three-dimensional time and frequency-domain theory of femtosecond x-ray pulse generation through Thomson scattering". en. In: *Phys. Rev. Spec. Top. - Accel. Beams* 7.6 (June 2004).
[13] Takashi Tanaka. "SIMPLEX: simulator and postprocessor for free-electron laser experiments". en. In: *J. Synchrotron Radiat.* 22.5 (Sept. 2015), pp. 1319–1326.
[14] *RAY-UI: A user interface for RAY*. URL: https://www.helmholtz-berlin.de/forschung/oe/np/optik-strahlrohre/arbeitsgebiete/ray_en.html.
[15] *Libera BPM electronics*. URL: https://www.i-tech.si/products/libera-single-pass-e/.
[16] K Nakamura et al. "Pico-coulomb charge measured at BELLA to percent-level precision using a Turbo-ICT". In: *Plasma Phys. Control. Fusion* 58.3 (Mar. 2016), p. 034010.
[17] Michael Röhrs et al. "Time-resolved electron beam phase space tomography at a soft x-ray free-electron laser". In: *Phys. Rev. ST Accel. Beams* 12 (5 May 2009), p. 050704. DOI: 10.1103/PhysRevSTAB.12.050704. URL: https://link.aps.org/doi/10.1103/PhysRevSTAB.12.050704.
[18] H. Huck et al. "First results of commissioning of the pitz transverse deflecting structure". In: *37th International Free Electron Laser Conference (FEL 2015)*. Daejeon, Korea: JACoW, Aug. 2015.
[19] Dmitriy Malyutin. "Time resolved transverse and longitudinal phase space measurements at the high brightness photo injector PITZ". PhD thesis. Apr. 2014.
[20] A Chaleil et al. "Inverse Compton scattering X-ray source yield optimization with a laser path folding system inserted in a pre-existent RF linac". en. In: *Nucl. Instrum. Methods Phys. Res. A* 840 (Dec. 2016), pp. 113–120.
[21] Benedikt Günther et al. "Device for source position stabilization and beam parameter monitoring at inverse Compton X-ray sources". In: *Journal of Synchrotron Radiation* 26.5 (Sept. 2019), pp. 1546–1553. DOI: 10.1107/S1600577519006453. URL: https://doi.org/10.1107/S1600577519006453.
[22] *Si-pin diode*. URL: URL:https://www.hamamatsu.com/eu/en/product/opticalsensors/photodiodes/si-photodiodes%20/S3590-09.html.
[23] *CCD camera*. URL: URL:https://www.artisantg.com/Scientic/62599-3/Basler-AVA1600-50GM-Monochrome-Area-Scan-Camera.
[24] *XBPM*. URL: URL:https://fmb-oxford.com/products/detectors-diagnostics/beam-position-monitors/blade-bpm/.
[25] *Si-drift detector*. URL: URL:https://www.ketek.net/sdd/vitus-sdd-modules/.
[26] K Medjanik et al. "Direct 3D mapping of the Fermi surface and Fermi velocity". en. In: *Nat. Mater.* 16.6 (June 2017), pp. 615–621.
[27] K Medjanik et al. "Progress in HAXPES performance combining full-field k-imaging with time-of-flight recording". en. In: *J. Synchrotron Radiat.* 26.Pt 6 (Nov. 2019), pp. 1996–2012.
[28] D Kutnyakhov et al. "Time- and momentum-resolved photoemission studies using time-of-flight momentum microscopy at a free-electron laser". en. In: *Rev. Sci. Instrum.* 91.1 (Jan. 2020), p. 013109.
[29] "A high-pressure x-ray photoelectron spectroscopy instrument for studies of industrially relevant catalytic reactions at pressures of several bars". en. In: *Rev. Sci. Instrum.* 90.10 (Oct. 2019), p. 103102.
[30] Friso van der Veen and Franz Pfeiffer. "Coherent x-ray scattering". In: *J. Phys. Condens. Matter* 16.28 (July 2004), pp. 5003–5030.

[31] Felix Lehmkühler, Wojciech Roseker, and Gerhard Grübel. “From femtoseconds to hours—measuring dynamics over 18 orders of magnitude with coherent X-rays”. en. In: *Appl. Sci. (Basel)* 11.13 (July 2021), p. 6179.

[32] S Pfeiffer et al. “Design of an optimal and robust controller for a free-electron laser exploiting symmetries of the RF-system”. In: *2012 IEEE 51st IEEE Conference on Decision and Control (CDC)*. Maui, HI, USA: IEEE, Dec. 2012.

[33] S Schulz et al. “Femtosecond all-optical synchronization of an X-ray free-electron laser”. en. In: *Nat. Commun.* 6.1 (Jan. 2015), p. 5938.

[34] *ASU compact x-ray light source*. URL: https://www.optica.org/en-us/events/meeting_archives/2018/compact_(euv_x-ray)_light_sources/.

[35] V. Petrillo et al. “Polarization of x-gamma radiation produced by a Thomson and Compton inverse scattering”. In: *Phys. Rev. ST Accel. Beams* 18 (11 Nov. 2015), p. 110701. DOI: 10.1103/PhysRevSTAB.18.110701. URL: https://link.aps.org/doi/10.1103/PhysRevSTAB.18.110701.

[36] Hongze Zhang. “Experimental polarization control of Thomson scattering X-ray source”. In: JACoW, Geneva, Switzerland, Jan. 2018.

[37] E A Nanni and W S Graves. “Aberration corrected emittance exchange”. In: *Phys. Rev. Spec. Top. - Accel. Beams* 18.8 (Aug. 2015).

[38] E A Nanni, W S Graves, and D E Moncton. “Nanomodulated electron beams via electron diffraction and emittance exchange for coherent x-ray generation”. In: *Phys. Rev. Accel. Beams* 21.1 (Jan. 2018).

[39] W S Graves et al. “Nanopatterned electron beams for temporal coherence and deterministic phase control of x-ray free-electron lasers”. In: (2019).

[40] J G H Franssen et al. “Compact ultracold electron source based on a grating magneto-optical trap”. en. In: *Phys. Rev. Accel. Beams* 22.2 (Feb. 2019).

[41] B H Schaap et al. “Photon yield of superradiant inverse Compton scattering from microbunched electrons”. In: *New J. Phys.* 24.3 (Mar. 2022), p. 033040.